**NASA TECHNICAL NOTE**

**NASA TN D-7867**

NASA TN D-7867

```
(NASA-TN-D-7867)  A RADIOSONDE THERMAL                  N75-17043
SENSOR TECHNIQUE FOR MEASUREMENT OF
ATMOSPHERIC TURBULENCE (NASA)  44 p HC $3.75
                                   CSCL 04B             Unclas
                                                H1/47   09925
```

# A RADIOSONDE THERMAL SENSOR TECHNIQUE FOR MEASUREMENT OF ATMOSPHERIC TURBULENCE

*Jack L. Bufton*

*Goddard Space Flight Center*
*Greenbelt, Md. 20771*

NATIONAL AERONAUTICS AND SPACE ADMINISTRATION • WASHINGTON, D. C. • FEBRUARY 1975

**1. Report No.** NASA TN D-7867

**2. Government Accession No.**

**3. Recipient's Catalog No.**

**4. Title and Subtitle**
A Radiosonde Thermal Sensor Technique for
Measurement of Atmospheric Turbulence

**5. Report Date** February 1975

**6. Performing Organization Code** 723

**7. Author(s)** Jack L. Bufton

**8. Performing Organization Report No.** G-7443

**9. Performing Organization Name and Address**
Goddard Space Flight Center
Greenbelt, Maryland 20771

**10. Work Unit No.** 502-23-15-30

**11. Contract or Grant No.**

**12. Sponsoring Agency Name and Address**
National Aeronautics and Space Administration
Washington, D. C. 20546

**13. Type of Report and Period Covered** Technical Note

**14. Sponsoring Agency Code**

**15. Supplementary Notes**

**16. Abstract**

A new system has been developed to measure vertical profiles of microthermal turbulence in the free atmosphere. It combines thermal sensor technology with radiosonde balloon systems. The resultant data set from each thermosonde flight is a profile of the strength and distribution of microthermal fluctuations which act as tracers for turbulence. The optical strength of this turbulence is computed and used to predict optical and laser beam propagation statistics. A decription of the flight payload, examples of turbulence profiles, and comparison with simultaneous stellar observations are included.

**17. Key Words (Selected by Author(s))**
Atmospheric turbulence,
Optical propagation,
Scintillation, Laser propagation,
Turbulence measurement

**18. Distribution Statement**
Unclassified–Unlimited
CAT. 47

| | | | |
|---|---|---|---|
| **19. Security Classif. (of this report)** | **20. Security Classif. (of this page)** | **21. No. of Pages** | **22. Price*** |
| Unclassified | Unclassified | 40 | $3.75 |

*For sale by the National Technical Information Service, Springfield, Virginia 22151.

# CONTENTS

*Page*

# A RADIOSONDE THERMAL SENSOR TECHNIQUE FOR MEASUREMENT OF ATMOSPHERIC TURBULENCE

Jack L. Bufton
*Goddard Space Flight Center*

## INTRODUCTION

In the past few years increased interest in propagation effects in the free atmosphere at microwave and optical frequencies has encouraged the study of microscale turbulence. Even in clear air the density inhomogeneities resulting from turbulent mixing tend to scatter incident radiation. The resulting phase and amplitude degradation of the propagated radiation can lead to serious problems for radar and communication links. Theory relating turbulence structure to propagation statistics is generally available for the interesting propagation paths but, until recently, little turbulence data had been gathered. This lack of data is especially severe for the atmosphere beyond a few tens of meters above ground level. Early attempts to collect these data concentrated on profiles and the spectra of temperature, wind velocity, energy dissipation rate, etc. Turbulence theory was then required to convert the data into a strength factor for prediction of propagation statistics. Recently, remote sensing techniques of radar backscatter and optical correlation have been used or proposed to infer the necessary profiles of the turbulence strength factor. Other recent efforts have concentrated on direct point measurement of this strength by using temperature structure as a tracer for turbulence structure. Typical results of these efforts are the data reported by Tsvang[1] and Lawrence, Ochs, and Clifford[2] on the strength of microthermal fluctuations in the free atmosphere to heights of a few kilometers. The work reported here combines the thermal sensor technology for microthermal measurements with radiosonde balloon systems. The result is an extension of turbulence sensing for the first time to heights up to 25 km above sea level. The result is a complete vertical profile of microscale turbulence structure for use in analysis of space-to-earth and earth-to-space propagation links. The measurement system is here referred to as the thermosonde (thermal sensor radiosonde) system. Thermosonde data provide the quantitative link between theory and propagation statistics. The data may also be used to infer the large scale turbulence structure known as CAT (clear air turbulence), which adversely affects aircraft operations.

In the thermosonde system a pair of high resolution thermal sensors and the associated electronics report temperature statistics by telemetry during both balloon ascent and descent. The prototype payload instrumentation was tested during October 1970 and again during September 1971, in conjunction with an earth-to-balloon laser propagation experiment at White Sands Missile Range, New Mexico. The thermosonde payload was reeled down from the main balloon payload to gather turbulence data for analysis of the laser propagation results. Details of the prototype payload plus examples of the turbulence profiles are reported by Minott, Bufton, and Fitzmaurice[3] and by Bufton et al.[4] The production thermosonde payload is an improved light-weight, low-cost version of the prototype. Because of these improvements it is suitable for use with standard radiosonde balloon systems. Both the prototype and the final payload version were developed and produced by GTE-Sylvania under contract to the Laser Technology Branch, GSFC.

This report will present specifications and operation details of the final thermosonde payload. The turbulence profile data collected will be presented and discussed in light of the temperature and wind velocity fields for the area of each flight. Applications of the turbulence profiles to analysis of optical propagation results will also be discussed in detail. In particular the results of near simultaneous stellar observations and thermosonde flights are compared. The major motivation for this comparison as for the thermosonde development program itself was the desire to monitor atmospheric turbulence effects at high altitude on laser communication links. Progress toward this goal and other applications of the thermosonde data are discussed in the comments section.

## DESCRIPTION OF THERMOSONDE SYSTEM

### Theory of Measurement

The fluctuations in refractive index that result from turbulent mixing are quite random in nature and are best described by statistics. The fundamental statistical quantity is the structure function and its strength factor, the structure coefficient.

Turbulence strength and distribution enters optical propagation theory through $C_N^2(h)$, the refractive-index structure coefficient. Propagation statistics invariably contain integrals over this turbulence strength factor as it varies with altitude h. For optical frequencies, $C_N^2(h)$ depends almost entirely on microscale temperature fluctuations specified by the temperature structure coefficient, $C_T^2(h)$. The connection at a wavelength of 0.5 $\mu$m is provided by

$$C_N^2(h) = \left[\frac{80\ P(h)}{T(h)^2} \times 10^{-6}\right]^2 C_T^2(h), \qquad (1)$$

where P(h) = pressure (mb) and T(h) = temperature (K). The thermosonde system provides $C_T^2(h)$ data and thus $C_N^2(h)$ data by measuring mean square temperature fluctuations as a function of altitude and using the widely accepted Obukhov[5]-Kolmogorov[6] turbulence theory,

$$C_T^2\ (h) = \left\{\frac{[T(\vec{r}_1) - T(\vec{r}_2)]^2}{r^{2/3}}\right\}_h , \qquad (2)$$

where $r = |\vec{r}_2 - \vec{r}_1|$ .

This theory requires isotropic turbulence structure, and is applicable for turbulence element sizes (r) larger than $l_i$, the inner scale, and smaller than $l_o$, the outer scale. Turbulence elements between these scale sizes comprise the inertial subrange. Energy input to the turbulence process through structures of dimension $l_o$ cascades down adiabatically through the inertial subrange until it is lost as heat in structure of dimension less than $l_i$. Tsvang[1] and others have indicated that the existence of an inertial subrange and the validitv of the 2/3-power law are well supported by field measurement. The assumption of isotropy indicated above must be modified to one of local isotropy, since turbulence strength and scale sizes $l_o$ and $l_i$ are expected to vary with altitude. Thus in equation (2), altitude, h, is indicated as a parameter of the measurement. The scale size $l_i$ is on the order of a few cm near the surface and increases to tens of cm in the stratosphere. The outer scale $l_o$ is thought to be roughly equal to altitude above the surface. The scale sizes which most affect the optical propagation generally fall within these inertial subrange limits at all altitudes and are weighted most heavily towards those near $l_i$ The end result of the microthermal measurements when expressed in terms of refractive index statistics is $C_N^2$. Its variations with altitude constitute a vertical profile of the optical strength of turbulence.

## Details and Specifications of the Thermosonde System

The thermosonde payload is used to measure root mean square (rms) temperature difference between two fine platinum wires, and to send the result over telemetry to a ground receiver station. Each platinum wire probe is 2.5 $\mu$m in diameter and about 6 mm long. They have a linear resistance-temperature coefficient, and respond to an increase in atmospheric temperature with an increase in resistance. For a temperature change, $\Delta T$, of 1.0 K a typical resistance change, $\Delta R$, is near 0.3 ohm. Resistance changes accurately follow temperature changes at frequencies from dc to near 1 kHz. The two probes are mounted parallel to each other and separated by 1.0 m in the horizontal plane. Each fine wire probe is soldered to two stiff wires about 8 cm long, which are in turn soldered to a printed circuit card. When the two cards are attached to polyurethane support arms the distance between probes is 1 m.

The probes are connected as two arms of a Wheatstone bridge. This permits a sensitive measure of temperature difference. The bridge is driven by a 3-kHz oscillator. The bridge output carrier signal is amplitude-modulated by the temperature difference signal. Figure 1 is a block diagram of the bridge temperature measurement scheme, the electronics for computing mean square temperature difference, and the telemetry transmitter.

The bridge output voltage is amplified, bandpass filtered and synchronously detected. After demodulation, the signal is low-pass filtered to 1 kHz, then sent through an rms operator module with a 5-second RC output time constant. The result is a voltage proportional to root mean square temperature difference. Calibration of this output is achieved before flight by temporarily inserting a reference resistor into the bridge network. A feedback system senses the

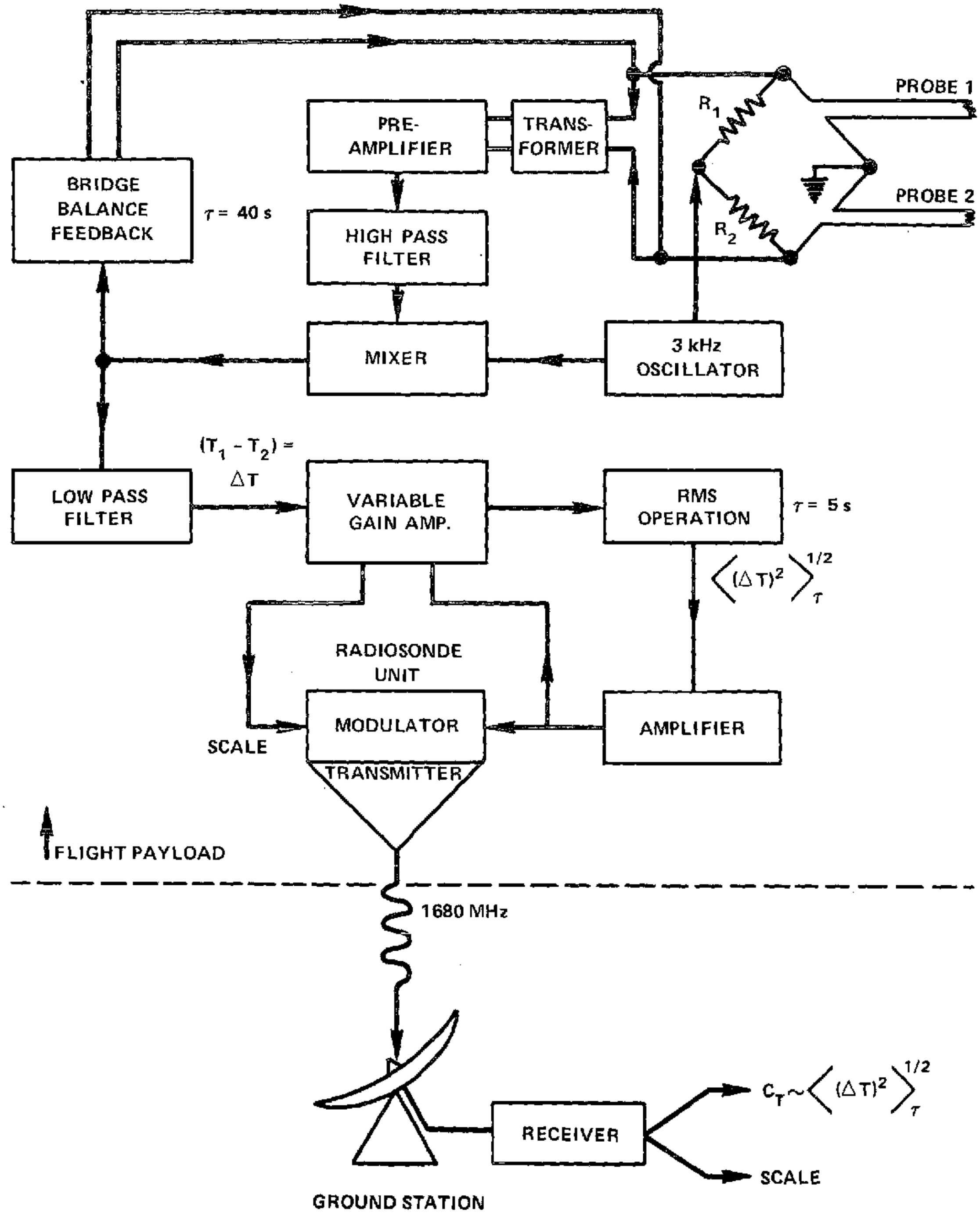

Figure 1. Thermosonde Signal Processing Electronics

average $\Delta T$ voltage and selects unity gain or 13X gain at the input to the rms module. Gain switching effectively increases the dynamic range of rms measurement to 44 dB from 0.004 K (system noise level) to 0.676 K. The system noise level yields a $(\Delta T)^2$ of $1.6 \times 10^{-5}$ $K^2$ and from equation (2) with r = lm, $C_T^2 = 1.6 \times 10^{-5}$ $C^2 m^{-2/3}$. This in turn with equation (1) implies a typical noise level for $C_N^2(h)$ of $1.6 \times 10^{-17}$ $m^{-2/3}$ at surface level; $2.9 \times 10^{-18} m^{-2/3}$ at h = 10 km and $1.4 \times 10^{-19} m^{-2/3}$ at h = 20 km. Another feedback loop corrects for bridge imbalance over an RC time constant of 40 seconds. Long term imbalance could result from small differences between resistance-temperature coefficients of the probes, and the typical ambient temperature changes from 290 K near the surface to 200 K at 10 km altitude. Because of this feedback loop the low end response to temperature changes does not extend entirely to dc. The net accuracy for rms computation is within ±10 percent for the extremes of turbulence and ambient temperature indicated above.

Rms output is sent along with a dc voltage indicative of gain scale to the telemetry transmitter. The telemetry system is a standard Weather Service frequency-modulated 1680 MHz system with transmitter modified to have a linear response to input voltage over a 46-dB dynamic range and to delete the standard temperature and relative humidity data. Rms temperature fluctuation data are sent back continuously as the payload ascends and descends except for brief interruptions controlled by a pressure activated commutator during which scale information is transmitted.

The entire telemetry system was calibrated by applying a voltage equal to $\Delta T_{max}$ of 0.676 K and one equal to $\Delta T_{min}$ of 0.004 K to the transmitter. At the receiver, the output, which appears on chart paper, was adjusted to properly record these high and low limits. The received rms temperature difference data are squared to obtain $C_T^2$ (h) and thus $C_N^2$ (h).

Figure 2 is a photograph of an actual flight-configured thermosonde payload. The two thermal sensor probe supports, visible at either end of the horizontal arm, are separated by one meter. The rms signal processing electronics are located on a printed circuit board, which is approximately 20 cm square. The board is mounted vertically in the central portion of the payload. Pieces of polyurethane thermal insulation 3.8 cm thick enclose and protect the electronics, and form the probe support arm. Because of the insulation, temperature extremes inside the payload are confined to 273 ± 25 K for a typical flight. A typical probe support is composed of two 16-gauge bus wires, soldered to a printed circuit card strip. Horizontal probe mounting plus the thin rectangular shape of the payload tend to align the probes perpendicular to any air flow. The radiosonde modulator/transmitter is housed in the rear section of the payload. A battery supplying the + 115V and + 6V needed to operate this part of the system is also located in the rear section. The battery supplying ± 18V to the rms electronics and probe circuits is strapped to the top of the payload. Both batteries are activated by immersion in water just prior to launch, and provide approximately 3 hours of continuous operation.

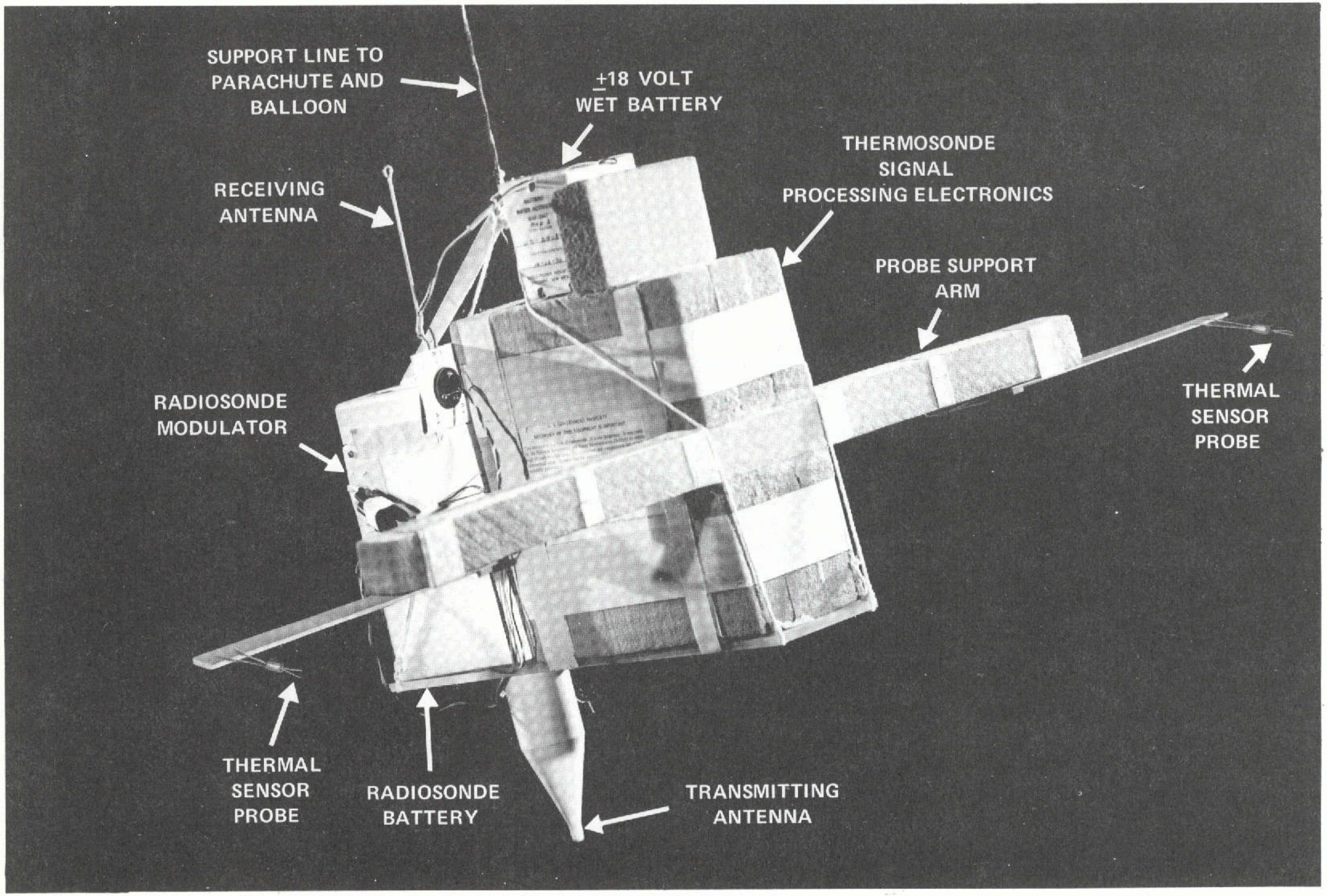

Figure 2. Thermosonde Flight Payload

The thermosonde payload is mounted approximately 5 meters below the parachute and approximately 55 meters below the radiosonde balloon. This is done to minimize balloon wake effects on the turbulence data during the ascent phase. Total payload weight is just under 2600 grams. Of that total, the major parts are activated batteries (920 gm), processing electronics (454 gm), and radiosonde transmitter (480 gm). Table 1 is a summary of the thermosonde performance specifications. The thermosonde system final report prepared by Titterton, Mallery, and Arken[7] at GTE-Sylvania contains a detailed collection of payload specifications.

Table 1

Thermosonde System Specifications

Parameter measured: $\left\langle (\Delta T)^2 \right\rangle_\tau^{1/2} \Rightarrow C_T^2$

Measurement time constant ($\tau$): 5 seconds

Measurement range: $0.004\ \mathrm{K} \leqslant \left\langle (\Delta T)^2 \right\rangle_\tau^{1/2} \leqslant 0.676\ \mathrm{K}$

$\Delta$T noise level: 0.004 K maximum

$\Delta$T saturation level: 2.0 K

Frequency range of $\Delta$T measurement: 0.16 Hz to 1.0 kHz

Thermal sensor probe:
- diameter: 2.5 µm
- length: 6 mm
- material: platinum
- separation: 1 m

Balloon ascent rate: 5 m $s^{-1}$

Payload descent rate: 10 m $s^{-1}$

Maximum altitude: 25 km

Turbulence structure vertical resolution:
- 25 m (ascent)
- 50 m (descent)

Payload weight: 2600 gm

Telemetry frequency: 1680 MHz

Battery power requirements: ±18 V at 175 mA, + 115 V at 45 mA, +6 V at 300 mA

Typical mission duration: 2.5 hours

A typical thermosonde mission profile would include the following:

1. Battery activation and telemetry calibration before launch.
2. Ascent at 5 $m\ s^{-1}$ to an altitude above 20 km.
3. Separation of payload and balloon by firing of explosive cutter at a predetermined time interval after launch.
4. Payload descent by parachute at 10 $m\ s^{-1}$ until surface impact.

During the flight, the balloon and payload follow a trajectory dictated by the mean wind structure. Microthermal turbulence data are sent by telemetry on both ascent and descent. The product of balloon vertical speed and the rms time constant (5 seconds) yields a turbulence element resolution of 25 m on ascent and 50 m on descent. Thus, the reported rms temperature data at any instant of time reflects an average over the last 25 or 50 meters.

### Error Mechanisms

There are several readily identifiable sources of error inherent in the thermosonde turbulence measurement technique. As mentioned above the system noise level is at or below $\Delta T =$ 0.004 K. This is the point where signal-to-noise ratio (SNR) = 1.0. Data accuracy increases for $\Delta T$ above this value in proportion to signal strength. For $\Delta T = 0.4$ K, SNR = 40 dB and the measurement error is on the order of 1 percent. Additional error bounds of ±10 percent were noted above for the rms computation. It is estimated that telemetry errors and reading errors at the ground station are considerably less than this ±10 percent. After received data is squared to obtain $C_T^2(h)$ and thus, $C_N^2(h)$, the error is on the order ±20 percent. Since the turbulence coefficients $C_T^2(h)$ and $C_N^2(h)$ are expected to vary over several orders of magnitude, this error is not of major proportions.

As noted above, the turbulence element resolution was limited to 25 m on ascent and 50 m on descent. There is strong evidence from radar probing that the minimum vertical extent of some turbulence layers may be only a few meters. Any such fine structure in the turbulence profile would not be apparent in detail in the thermal sensor data, but would of course contribute to the 5-second integrated value for $C_T^2(h)$.

The temperature measurement of the sensors may be in error due to a variety of factors in the heat exchange of each sensor with the air, radiation field, and support structures. Heat exchange errors would be significant only when they have different relative effects on each sensor. This is because temperature difference, not absolute temperature, is the parameter measured. A likely candidate for differential error is daytime solar radiation.

During the ascent portion of the flight, air flow over the balloon and payload may break into turbulence, and thus cause the thermal sensors to report higher turbulence strengths. The most serious wake effects should occur at high altitude, where the temperature differential between balloon and atmosphere contributes thermal eddies to the wake. For this reason descent data will be used to predict the optical effects. Unfortunately the descent profiles do not include data in the first 1 or 2 km above mean sea level (MSL) because of telemetry dropouts. Thus it will be necessary to use some ascent data to have a complete profile for comparison with the optical data.

Turbulence non-stationarity also affects the quality of the thermal sensor data, and in particular its usefulness in computing optical propagation statistics. Although it is helpful that major turbulence layers and features often are visible on both ascent and descent profiles, even though the profiles are separated by tens of minutes and tens of kilometers, the fact remains that thermosonde data result from point measurements of structure changing in both time and space. For effective correlations with propagation data it is essential that the turbulence data be acquired simultaneously and that the balloon flight path be near the propagation line of sight.

A more serious source of error may be the possible departure of the turbulence spatial spectrum from the classical Obukhov-Kolmogorov (-5/3) power law for wave number. This theory implies the existence of an inertial subrange of turbulence element sizes for which the turbulence is assumed to be, at least locally, isotropic and homogeneous. For well developed turbulences, a large amount of evidence supports this description. However, for a developing turbulence and for the breaking wave motion characteristic of upper altitude turbulence structure, another power law may apply. In addition, the limited vertical extent of some observed structure indicates a small outer scale, $l_0$, and truncation of the inertial subrange. The major effect of this error source would be to alter the quantitative prediction of optical effects.

Despite these rather serious qualifications of the observed data, the fact remains that the thermal sensor data are a fairly accurate point measurement of the temperature structure function for the spatial separation of one meter. As such, the data serve as at least a relative indication of the optical strength of turbulence, and a quite accurate indication of turbulence location.

## MICROTHERMAL TURBULENCE DATA

### Thermosonde Data Collection

Turbulence data were obtained with the prototype thermosonde payload during October 1970 and again during September 1971, as mentioned in the introduction. These flights were conducted as part of the Balloon Atmospheric Propagation Experiment (BAPE) at White Sands Missile Range (WSMR), New Mexico. One low-altitude turbulence profile was obtained during BAPE I (1970). This result, plus an illustration of the application of turbulence data to the laser propagation problem, is contained in the BAPE I final report.[3]

During BAPE II (1971) four turbulence profiles up to 15 km above MSL were obtained. All flights were from the runway of Holloman Air Force Base near Alamogordo, N. M.

The base is located on the desert floor, 1.2 km above MSL, and is bordered 50 km to the west by the San Andres mountains and 20 km to the east by the Sacramento mountains. Both mountain chains run north-south and rise 1 to 2 km above the desert floor.

The vehicle was a polyethylene balloon of 40-m diameter, which carried aloft a 450-kg optical-propagation experiment payload. The complete thermal sensor system weighed less than 45 kg,and was lowered on a nylon cord 300 m beneath the main payload when the balloon reached an altitude of 1 km. The purpose of lowering it was to minimize the balloon-wake effects on the thermal sensor measurement of turbulence as the balloon ascended 5 m $s^{-1}$. All launches were at dawn, in order to have minimum surface winds at the launch site. Thus, all data are for turbulent conditions before, during, and up to one hour after sunrise.

Turbulence data from BAPE II are reported by Bufton et al.[4] Unfortunately, no laser propagation data were available for comparison with the thermosonde results. Instead, major emphasis was placed on correlation of turbulence activity with indications of turbulence suggested by standard meteorological profiles of ambient temperature and wind velocity. These correlations are reported in detail by Bufton[8] and described in the next section.

The production version thermosonde payload was first test flown from Chico, California by GTE-Sylvania as part of the development program. Thermal sensor data were successfully recorded, and the major part of the payload was recovered intact after it had been floating in the Pacific Ocean for several days. Subsequent flights of the production model, from which data have been recorded and reduced, were launched at the Goddard Optical Research Facility (GORF), located near Beltsville, Maryland. This launch site has an elevation of about 50 m above mean sea level, with local terrain characteristic of rolling, partially wooded coastal plain. The data presented here were obtained under nighttime or daytime conditions on several occasions from May to October, 1972. Most launches were conducted just after dusk or dawn in order to minimize winds at launch. About 60 percent of the flight payloads were recovered, returned to GSFC for refurbishment, and flown again.

Both the prototype flights at WSMR and the production version thermosonde flights at GORF were accompanied by standard radiosonde measures of upper air temperature and wind velocity profiles. At WSMR the radiosonde launches were within a two km horizontal distance and within one hour of the main balloon launch. The GORF flights were conducted within 1 to 2 hours of the National Weather Service radiosonde flight from Sterling, Virginia. The Sterling launch site is some 50 km due west of GORF. In both cases the thermosonde and standard radiosonde balloons followed similar trajectories dictated by the mean wind structure. Thus, both types of sensors sampled nearly the same volume of air.

### Data Reduction

The baseband output of the 1680-MHz ground-based receiver formed the basic thermosonde data set. This output was a voltage proportional to rms temperature fluctuations and was recorded continuously on a single-channel chart recorder. The event marker of this recorder was connected to the slow code output of a time code generator. This provided a time base (in universal time) which was updated every minute and permanently recorded alongside the thermosonde data. The chart record was 11.4mm wide with 50 equal divisions. Deflections on the chart record were linear with applied voltage, and by virtue of the payload electronics and modifications to the radiosonde modulator/transmitter were linear with rms temperature fluctuations. Final calibration about two minutes prior to launch was used to establish rms temperature reference levels on the chart record. Two references were selected by alternately shorting wires on the thermosonde payload. The low reference was used to simulate the thermal sensor noise level. For this the chart recorder pen was adjusted to 0 divisions. High reference simulated the maximum output $\Delta T$ rms = 0.676 K. Chart recorder gain was adjusted so that high reference occurred at 45 divisions (90 percent of full scale).

During the thermosonde flight, thermal sensor data were recorded continuously except for occasional interruptions by processing electronics gain scale information. These appeared as constant chart recorder levels, 25 percent of full scale for low gain and 60 percent of full scale for high gain. Scale indications last for several seconds, and were selected every 15 contacts on the pressure activated commutator of the radiosonde modulator/transmitter. The commutator calibration curve for contact number versus pressure (mb) was supplied with each unit. From this curve and the time history of contact number from the chart record, it was possible to plot pressure (mb) of the balloon payload versus time. This was converted into payload altitude (MSL) versus time by means of the standard radiosonde record of pressure versus altitude.

A thermosonde data point was selected for each 15-second interval of the chart record by visually averaging the raw data values and trends over that interval. Thus, one data point was available for each 75-m vertical section of the atmosphere on ascent, and 150-m section on descent. The 15-second interval included three time constants of the rms operation time constant aboard the payload. The selection of average points in effect digitized the raw analog chart record. The standard radiosonde data on upper air temperature and wind velocity were also digitized, but with coarser resolution (approx. 400 to 500 m). Both data sets were entered into a digital computer programmed to convert recorder divisions into rms temperature fluctuations, $C_T^2(h)$ and eventually $C_N^2(h)$, using the altitude-time curve, the temperature and pressure profiles, and the formulae of equations (1) and (2). The computer was also programmed to output integrals of the turbulence structure, compute optical propagation statistics, and permit rapid and accurate plotting of the input data and program results. Data presented below were all plotted in this manner.

## Thermosonde Turbulence Data

Figures 3 through 9 contain data from all thermosonde flights launched between 27 April 1972 and 10 October 1972, for which the raw thermal sensor data were reduced to profiles of $C_N^2(h)$. Thirteen flights were conducted in this series: Of the six flights for which no data are presented, three had in-flight problems with the processing electronics or the thermal sensors, two were system checkout flights with no data on descent, and one had a radiosonde telemetry failure. Both ascent and descent $C_N^2(h)$ profiles for each of the remaining seven flights are plotted in the figures. Ascent data for all flights indicated stronger turbulence with more layers than the corresponding descent profiles. The consistency of this effect suggests the presence of increased turbulence due to balloon wake on ascent. During descent by parachute there are no wake effects since the thermal sensors are the lead element.

The major characteristic of both ascent and descent $C_N^2(h)$ profiles is the irregular pattern of multiple spikes. Some of the spikes, or $C_N^2(h)$ maxima, are grouped together to form larger structures. Individual spikes, however, have a small vertical extent, often no larger than the thermosonde resolution of 25 to 50 m. Despite the ascent data bias due to wake effects, there is often good correlation between the larger structures visible on both ascent and descent profiles. Good examples are found at 10-11 km for flight 2, 9-10 km for flight 7, and 9-11 km for flight 9. The presence of correlation between individual spikes observed on both ascent and descent is somewhat rarer but still valid. Good examples are found at 7.3 km for flight 2, 2.2 km for flight 7, and 9.2 km for flight 9. The presence of even limited correlations argues for validity of the thermosonde measurement technique. It should also be realized that ascent and descent data sampling are typically separated by tens of minutes in time and kilometers in space. Thus, the degree to which correlation is present for turbulence structure at the same altitude argues for stationarity of the turbulence process and a large horizontal extent for a given structure. The combination of a small vertical extent and large horizontal extent suggests that the observed turbulence is in the form of layers or horizontal sheets. Lawrence, Ochs, and Clifford[2] noted similar stratification in microthermal measurements performed with aircraft up to an altitude of 3 km above ground level. Additional evidence for a multiple layered turbulence structure is contained in the radar backscatter measurements performed by Hardy and Katz[9] and Doviak, Goldhirsh, and Miller.[10] Their data showed frequent layers at a variety of altitudes up to and including the tropopause region. The layers of clear air turbulence seemed to be formed from wavelike structures that appear in horizontally stratified sheets. Measured wave amplitudes averaged around 500 m, with wavelengths on the order of kilometers. Higher resolution radar studies in the lower troposphere (near 300 m altitude) reported by Gossard, Jensen, and Richter[11] revealed turbulence structure as thin as several meters. Thus, the peaks in $C_T^2(z)$ visible in the present data are quite likely the result of a vertical cross section of thin horizontal turbulence sheets.

The strongest layers of turbulence of order $C_N^2(h) = 10^{-14}\,m^{-2/3}$ were generally confined to the surface boundary layer of about 10 m thickness. Other strong layers of order $C_N^2(h) = 10^{-16}\,m^{-2/3}$ were in the lower troposphere below 5 km and in the tropopause region 9 km and above. These two turbulent regions were separated by a relatively quiescent gap of about 4 km. The strongest turbulence layers were well correlated with inflections in the temperature profile, thin stable or inverted temperature layers, and regions of high wind shear. A more detailed comparison of meteorological parameters with the $C_N^2(h)$ data appears in the next section.

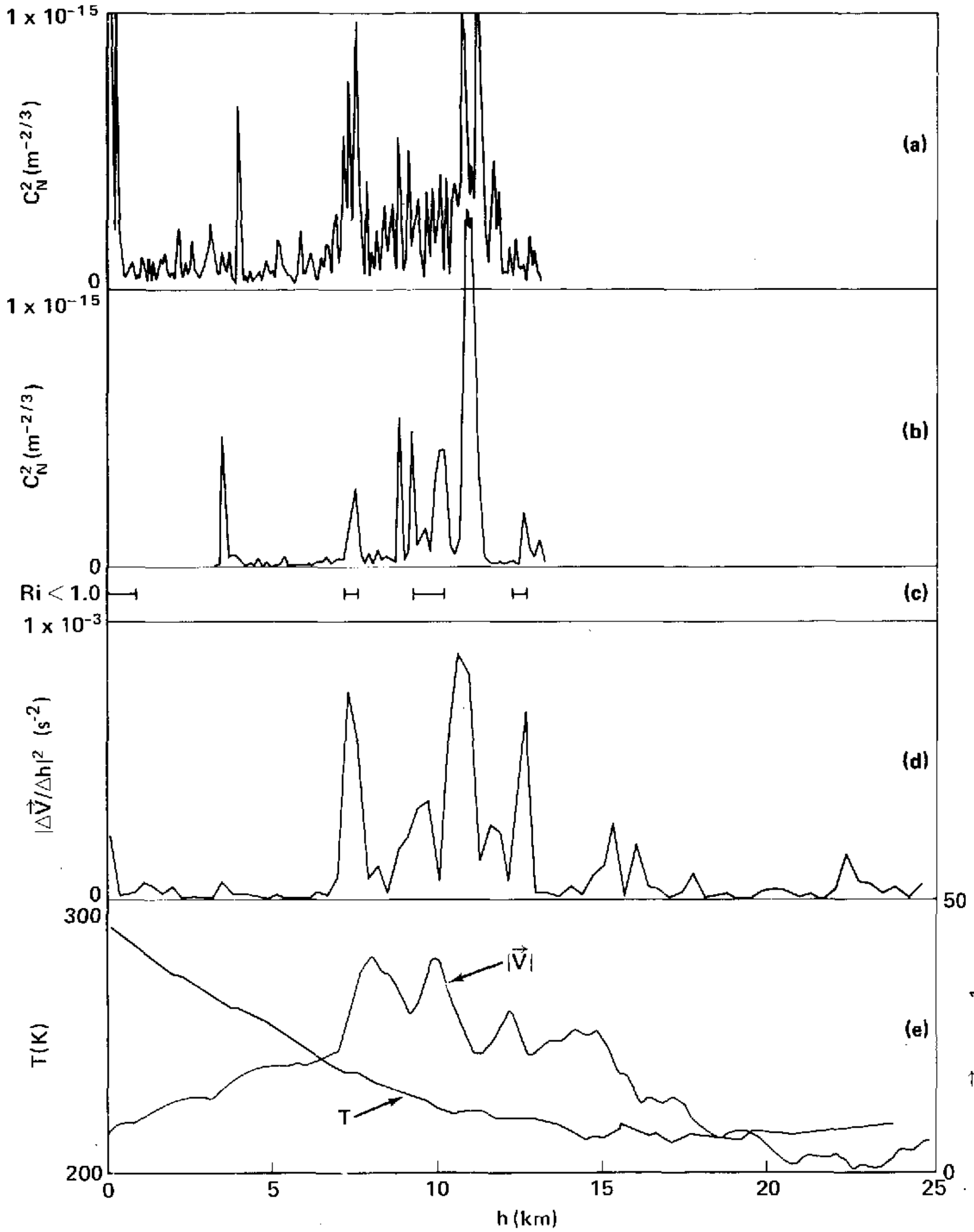

Figure 3. Data from Thermosonde Flight 2, 5 May 1972.

(a) Refractive-index structure coefficient $C_N^2$(h) ascent data.

(b) Refractive-index structure coefficient $C_N^2$(h) descent data.

(c) Low Richardson number (Ri < 1.0).

(d) Vector wind shear squared.

(e) Temperature T and wind speed v versus altitude above MSL.

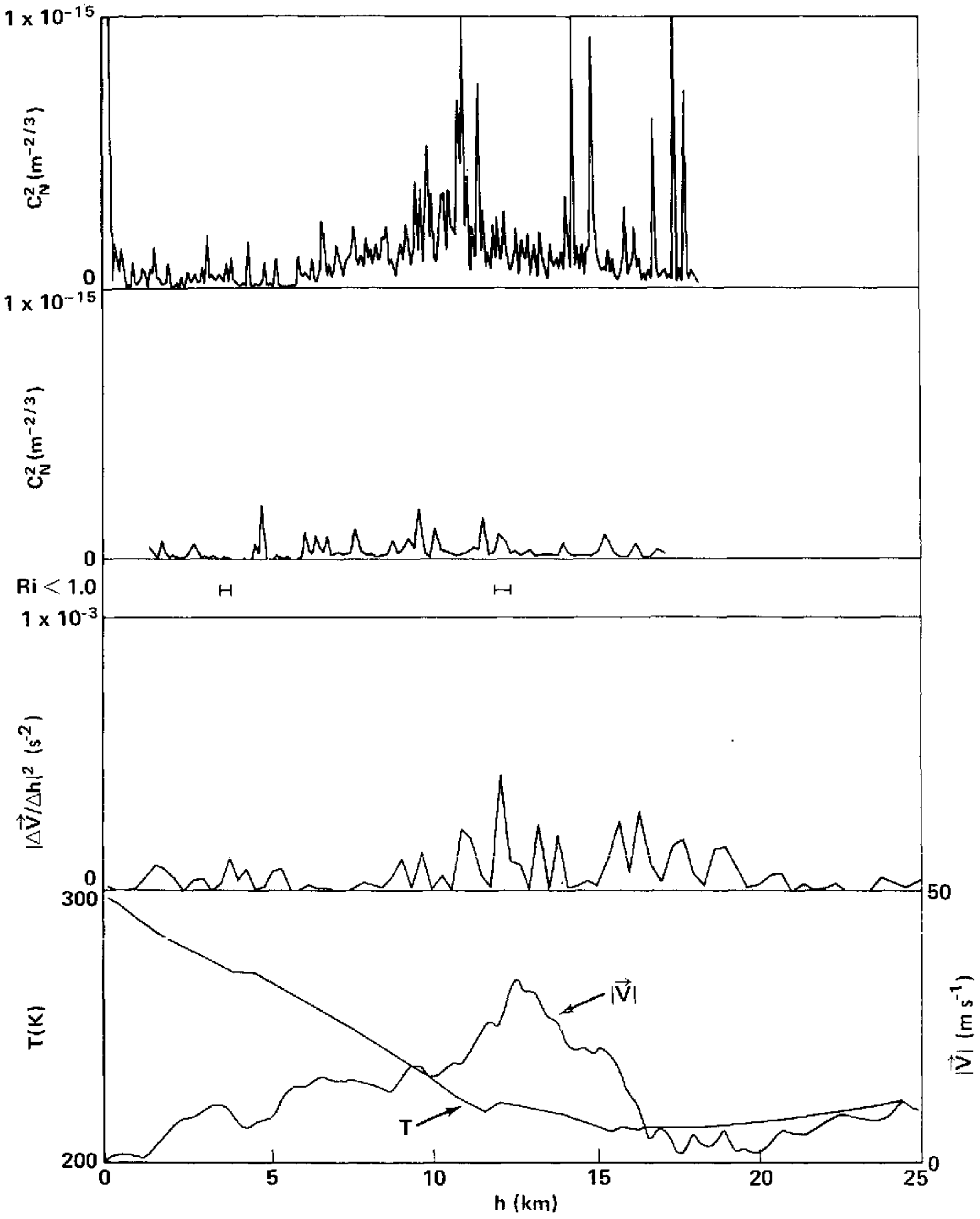

Figure 4. Data for Thermosonde Flight 4, 7 June 1972

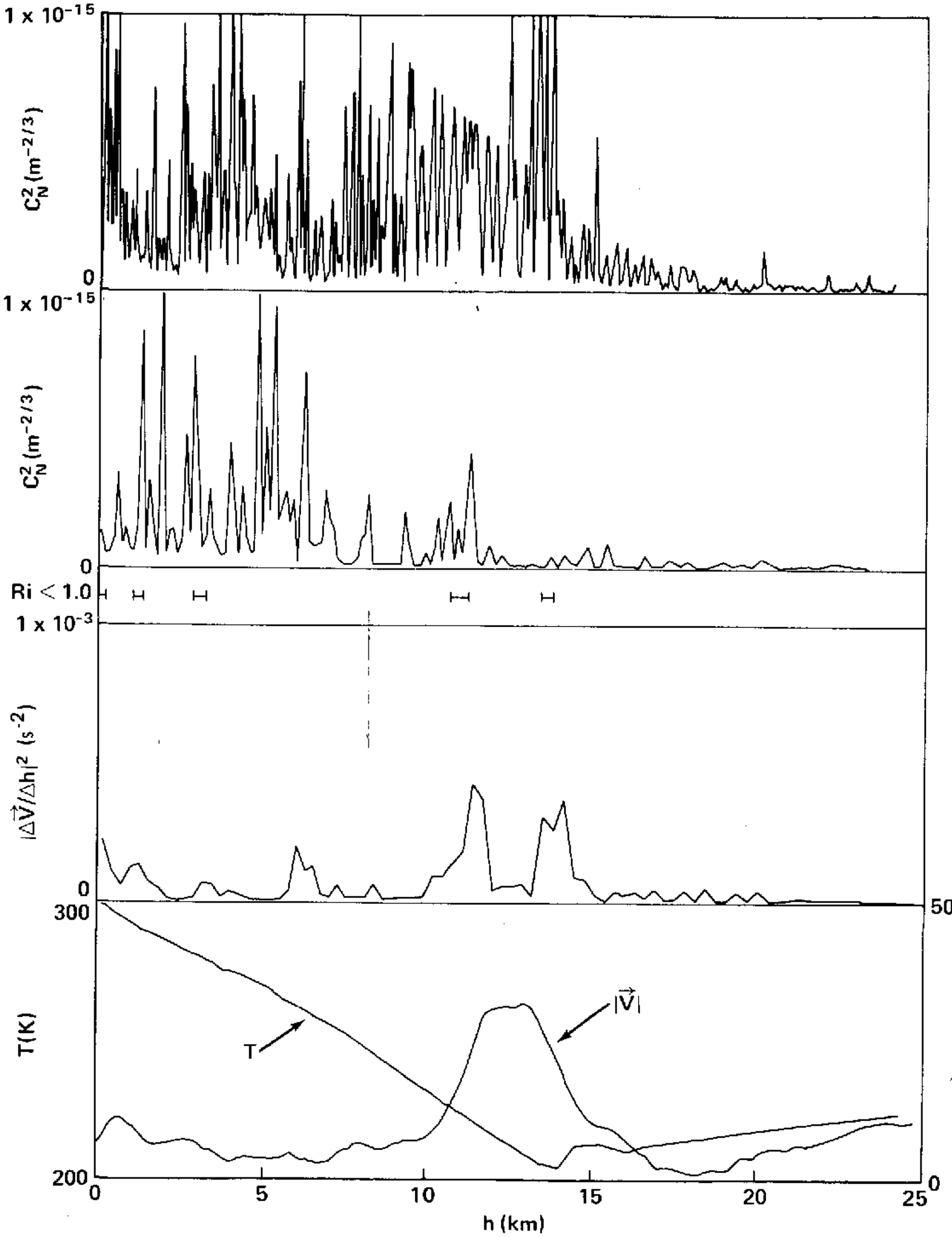

Figure 5. Data for Thermosonde Flight 5, 10 July 1972

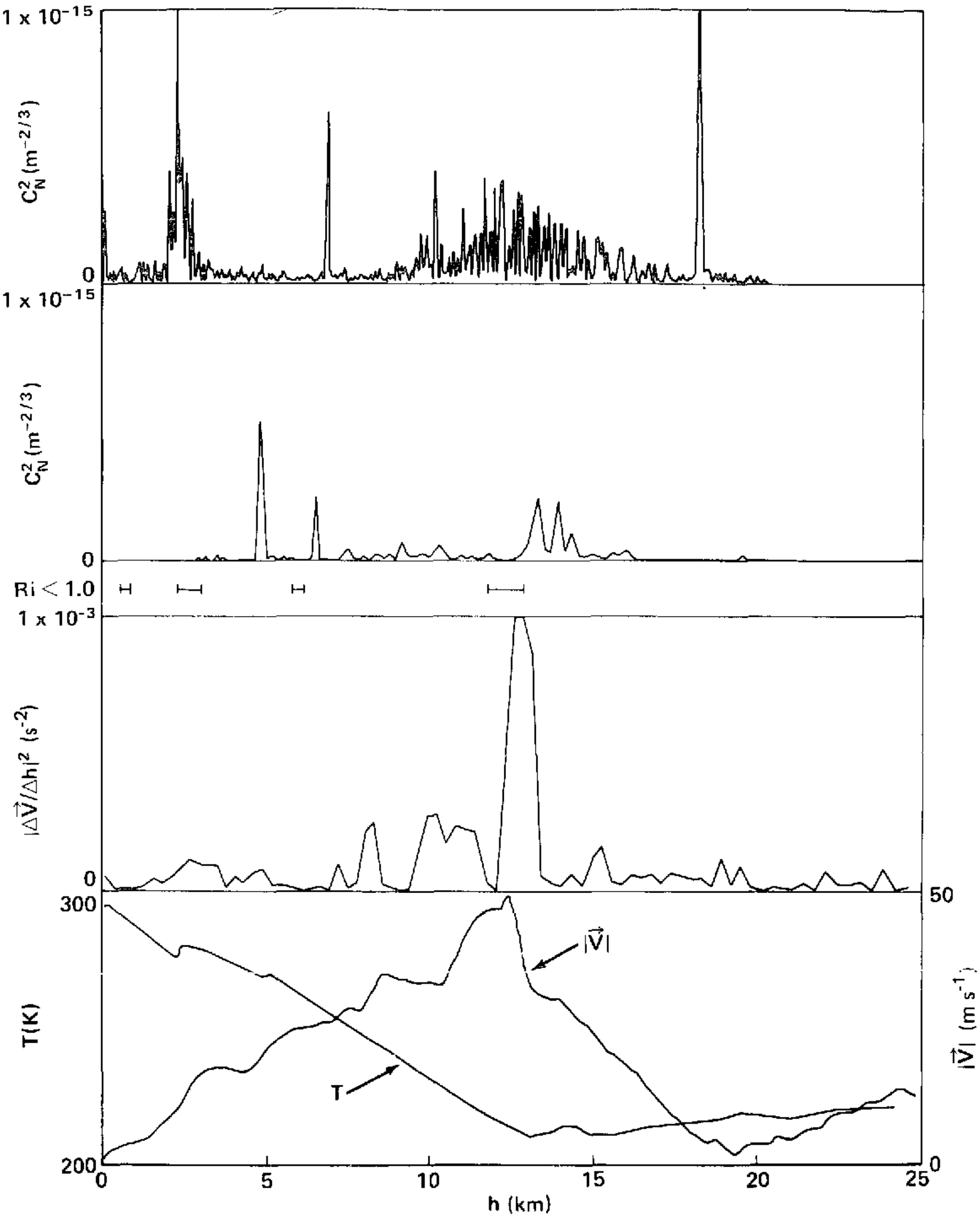

Figure 6. Data for Thermosonde Flight 6, 10 August 1972

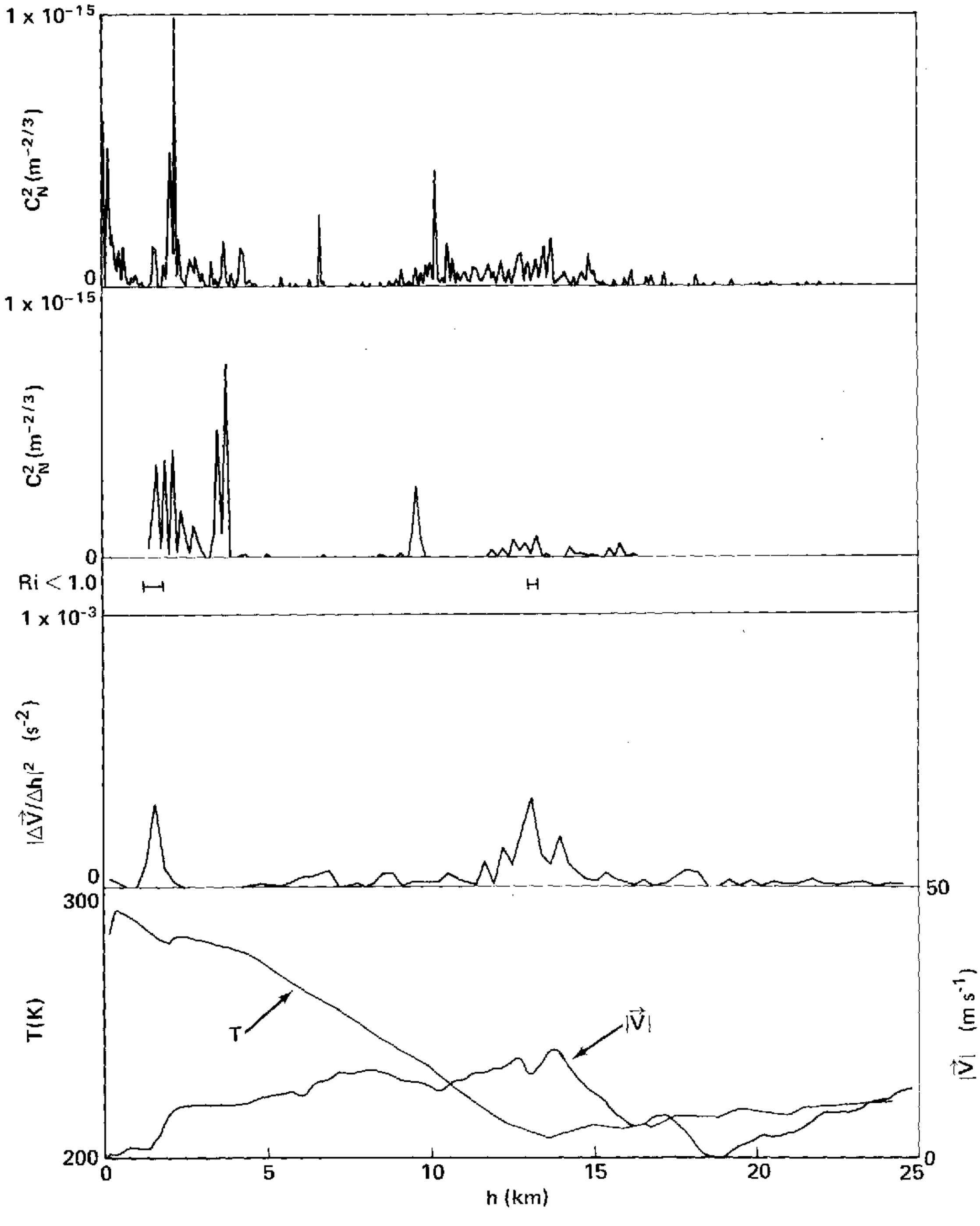

Figure 7. Data for Thermosonde Flight 7, 11 August 1972

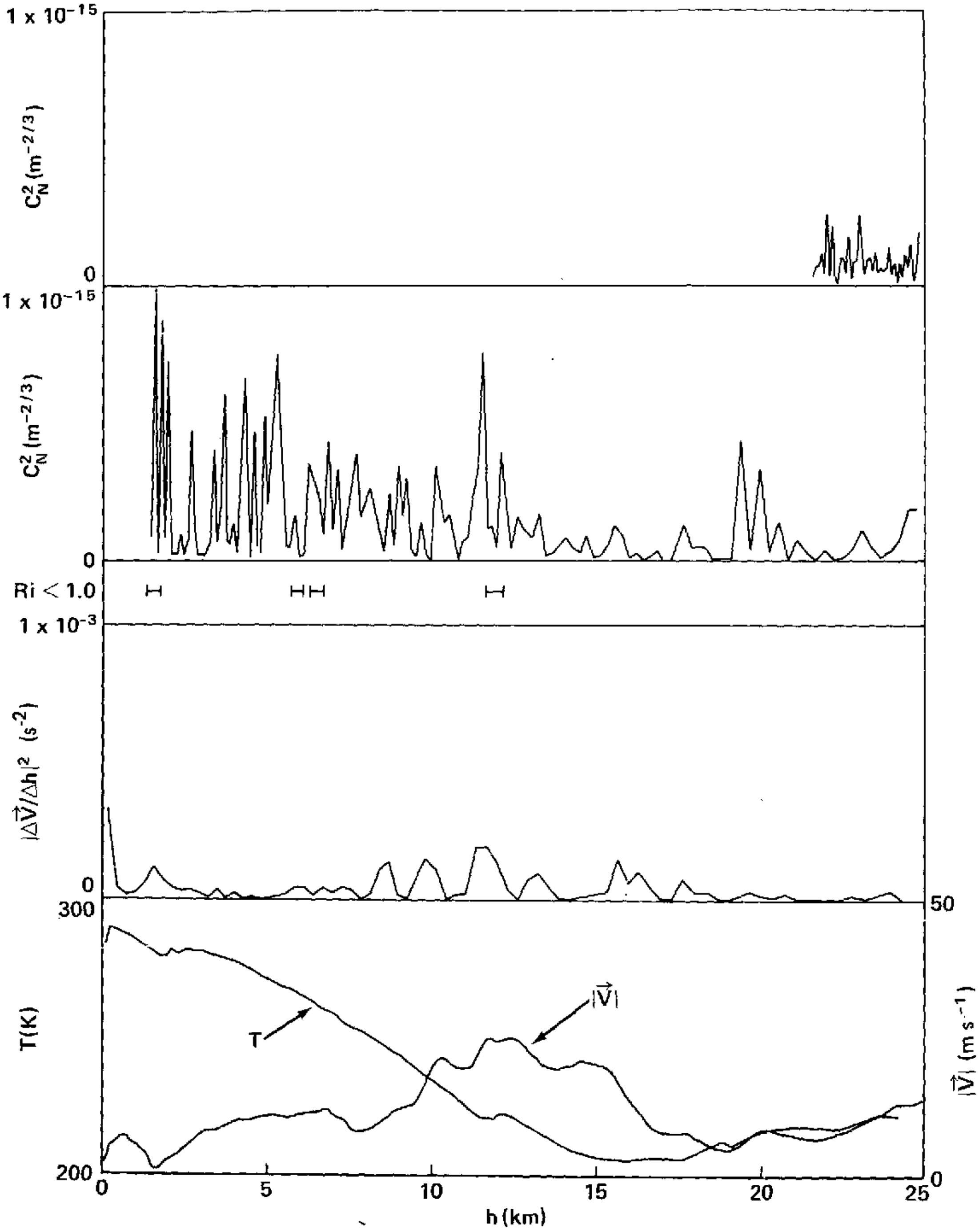

Figure 8. Data for Thermosonde Flight 8, 16 August 1972

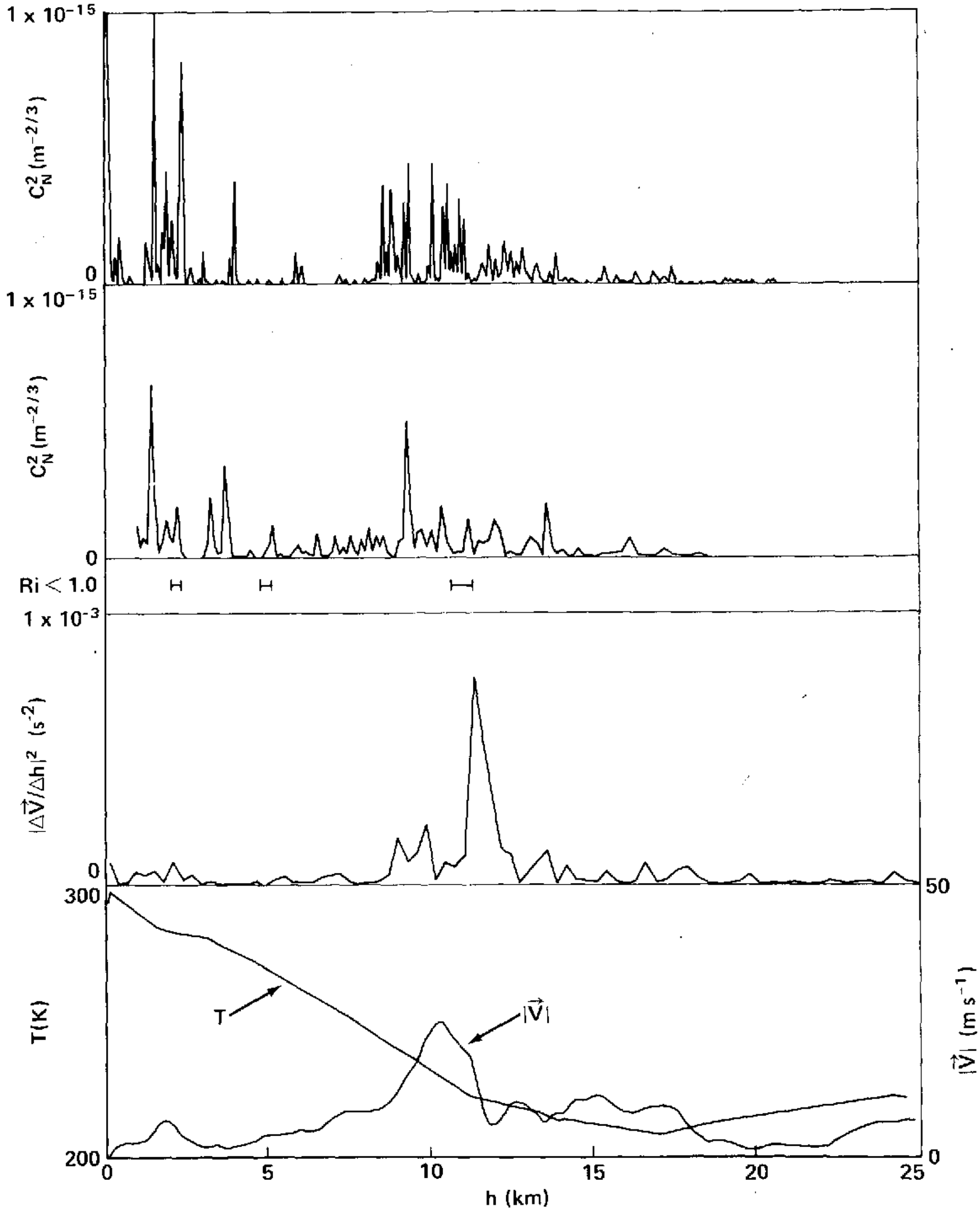

Figure 9. Data for Thermosonde Flight 9, 6 September 1972

## APPLICATIONS OF THERMOSONDE DATA

### Correlation with Meteorological Data

Upper altitude wind and temperature information from the standard radiosonde flights were plotted in figures 3 to 9, in order to provide background meteorology and to indicate correlations with the microthermal data. The wind field is specified by flow speed and direction. Wind speed profiles appear directly in the figures. Wind direction data are used along with speed information to compute vertical wind shear profiles. The shear is computed by numerical differentiation of vector wind vertical profiles. The vertical spacing between each pair of wind data points in the radiosonde record is approximately 300 m. This is the resolution element for shear computation. The magnitude of the vector difference between adjacent wind data points was divided by the 300-m interval to yield the vertical vector wind shear. A profile of the square of this shear appears in each figure. The radiosonde ambient temperature data were available only at relatively few significant levels, rather than the regular intervals of the wind data. Significant levels were chosen at those altitudes at which an inflection point occurred in the temperature vertical profile. Inflection points were stable, or inverted temperature lapse layers, or simple changes in temperature profile slope.

Spikes or layers in the $C_N^2(h)$ data appear to be well correlated with both temperature profile inflection points and vertical vector wind shear maxima. Good examples of this behavior are found at the 7.5- and 10.6-km levels in flight 2 and the 13.0-km level of flight 6. These correlations were achieved despite the separation of up to several hours and tens of kilometers between radiosonde and thermosonde flights. Often the temperature inflections and wind shear maxima were also well correlated with each other.

Table 2 provides a semi-quantitative view of these correlations. All major features of the temperature profile were listed along with the altitude, or altitude interval of occurrence. Major features included stable or inverted temperature layers and inflection points in the lapse rate. The vector wind shear and temperature structure coefficient profile were then examined by the author and the presence or absence of major features (maxima) in these profiles were recorded in the table. The major features in all profiles were rated as weak to moderate (○) or moderate to strong (●). In order for a major feature to be scored as present (correlated) with the temperature profile feature it had to be within ± 200 m of the temperature feature altitude in column 3 of table 2. Even the weak profile features were readily distinguishable by the height of their maxima above the average profile envelope. Note that $C_N^2(h)$ maxima are labeled with A or D for observations on ascent or descent, respectively.

### Table 2 (Sheet 1)
### Correlation of Turbulence and Meteorological Events

| Flight No. | Temperature | | | Wind Shear Presence and Intensity | Turbulence | |
|---|---|---|---|---|---|---|
| | Profile Feature † | Altitude or Altitude Range (km) | Feature Intensity * | | Presence and Intensity | Ascent (A) or Descent (D) |
| 2 | SL | 2.0– 2.4 | ○ | | | |
| | SL | 3.8– 4.0 | ● | ○ | ●/● | A/D |
| | ΔT | 5.0 | ○ | | | |
| | SL | 7.2– 7.6 | ● | ● | ●/○ | A/D |
| | ΔT | 9.7 | ○ | ○ | ● | D |
| | IL | 10.6–10.7 | ● | ● | ● | D |
| | SL | 10.7–11.4 | ● | ● | ● | A |
| | SL | 11.8–12.9 | ● | ● | ○ | D |
| | ΔT | 13.7 | ● | | | |
| 4 | ΔT | 1.5 | ○ | ○ | | |
| | SL | 3.8– 4.6 | ● | ○ | ○ | D |
| | ΔT | 7.4 | ○ | | | |
| | ΔT | 9.7 | ○ | ○ | ○/○ | A/D |
| | IL | 11.5–12.2 | ● | ● | ○ | D |
| | ΔT | 13.9 | ○ | ○ | | |
| | IL | 15.5–15.8 | ● | ● | ○ | D |
| | IL | 16.3–16.6 | ● | ● | ○ | A |
| | ΔT | 18.6 | ○ | ○ | | |
| 5 | SL | 1.3– 1.6 | ○ | ○ | ●/● | A/D |
| | ΔT | 3.8 | ● | | ● | A |
| | ΔT | 5.0 | ○ | | ● | D |
| | ΔT | 6.3 | ○ | ○ | ● | D |
| | ΔT | 7.6 | ○ | | | |
| | ΔT | 13.4 | ○ | ● | ● | A |
| | IL | 13.9–14.4 | ● | ● | ● | A |
| | ΔT | 15.2 | ● | | ○ | D |
| | IL | 16.0–16.6 | ● | | | |
| | ΔT | 21.0 | ○ | | | |
| 6 | IL | 2.2– 2.5 | ● | ○ | ● | A |
| | ΔT | 3.2 | ○ | ○ | | |
| | IL | 4.8– 5.1 | ● | ○ | ● | D |

† SL = stable temperature layer
IL = inverted temperature layer
ΔT = change in temperature gradient

* ○ Weak to moderate
● Moderate to strong

Table 2 (Sheet 2)
Correlation of Turbulence and Meteorological Events

| Flight No. | Temperature | | | Wind Shear Presence and Intensity | Turbulence | |
|---|---|---|---|---|---|---|
| | Profile Feature † | Altitude or Altitude Range (km) | Feature Intensity * | | Presence and Intensity | Ascent (A) or Descent (D) |
| | ΔT | 8.7 | ○ | ○ | | |
| | IL | 13.0–13.9 | ● | ● | ○/● | A/D |
| | SL | 13.9–14.3 | ◒ | ○ | | |
| | SL | 14.8–15.6 | ● | ○ | ○ | A |
| | IL | 15.6–16.6 | ● | | | |
| | ΔT | 17.7 | ○ | | | |
| | ΔT | 19.4 | ● | ○ | ○ | D |
| | IL | 20.9–22.3 | ● | | | |
| 7 | IL | 1.8– 2.2 | ◒ | ● | ●/● | A/D |
| | ΔT | 3.2 | ○ | | ● | D |
| | ΔT | 4.6 | ● | | | |
| | ΔT | 7.5 | ○ | | | |
| | ΔT | 9.8 | ○ | | ◒/◒ | A/D |
| | ΔT | 12.2 | ◒ | ● | ○ | D |
| | IL | 13.5–15.0 | ● | ● | ○/○ | A/D |
| | IL | 15.7–16.5 | ○ | ○ | ○ | D |
| | IL | 16.6–17.5 | ● | | | |
| | IL | 18.7–19.5 | ● | | | |
| | IL | 21.0–21.5 | ● | | | |
| 8 | ΔT | 0.8 | ○ | | | |
| | IL | 1.7– 2.5 | ● | ● | ● | D |
| | ΔT | 3.1 | ○ | | | |
| | ΔT | 4.0 | ○ | ○ | | |
| | ΔT | 4.9 | ○ | | ● | D |
| | ΔT | 6.0 | ○ | ○ | | |
| | ΔT | 7.1 | ○ | ○ | | |
| | ΔT | 7.6– 7.9 | ● | ○ | ○ | D |
| | ΔT | 9.4 | ○ | ● | ○ | D |
| | IL | 11.5–12.4 | ● | ● | ● | D |
| | ΔT | 14.0 | ○ | | ○ | D |
| | SL | 15.0–17.5 | ● | ◒ | | |
| | IL | 17.6–18.7 | ● | ○ | ○ | D |
| | IL | 19.1–19.8 | ● | ○ | ● | D |

Table 2 (Sheet 3)
Correlation of Turbulence and Meteorological Events

| Flight No. | Temperature | | | Wind Shear Presence and Intensity | Turbulence | |
|---|---|---|---|---|---|---|
| | Profile Feature † | Altitude or Altitude Range (km) | Feature Intensity * | | Presence and Intensity | Ascent (A) or Descent (D) |
| 9 | ΔT | 21.0 | ○ | ○ | ○ | D |
| | IL | 22.2–23.5 | ● | ○ | ○ | A |
| | ΔT | 1.2 | ○ | | | |
| | SL | 1.2 – 3.1 | ○ | ○ | ●/● | A/D |
| | ΔT | 5.1 | ○ | ○ | | |
| | ΔT | 9.5 | ○ | ● | ●/● | A/D |
| | ΔT | 11.2 | ● | ● | ●/○ | A/D |
| | ΔT | 12.0 | ○ | | ○/○ | A/D |
| | ΔT | 13.4 | ● | ● | | |
| | IL | 13.8–14.1 | ● | ○ | ○/○ | A/D |
| | IL | 17.0 | ● | | ○ | D |
| | ΔT | 18.6 | ○ | | | |
| | ΔT | 24.2 | ● | ○ | | |

The degree of correlation among the columns of table 2 is quite good. About 75 percent of the temperature features are correlated with either or both wind shear and $C_T^2(h)$ maxima. The best one-to-one correlation, 73 percent, appears between (●) temperature features and wind shear maxima. The second best correlation of 71 percent is between (●) temperature features and $C_T^2(h)$ maxima. The presence of wind shear at the altitude of a (●) temperature feature is found to essentially guarantee (87 percent correlation) the appearance of a (○) or (●) turbulence maximum. Thus both temperature profile features and wind shear maxima are found to be good predictors of turbulence activity at high altitude. A closer look at the data of table 2 reveals that the best correlations of the type noted above are found between 2 km and 10 km in the troposphere and at the tropopause.

Wind shear and temperature information, when combined to form a vertical profile of gradient Richardson number, provide a truly quantitative estimate of atmospheric fluid stability, and thus can lead to a prediction of the presence of turbulence activity. The gradient Richardson number,

$$\mathrm{Ri} = g \left(\frac{\partial T}{\partial h} + \gamma_a\right) \Big/ T \left|\frac{\partial \vec{V}}{\partial h}\right|^2 \tag{3}$$

is defined in terms of $g = 9.8\ \mathrm{m\ s^{-2}}$, temperature gradient $\partial T/\partial h$, adiabatic lapse rate $\gamma_a = +9.8\ \mathrm{K\ km^{-1}}$, temperature T(K), and vertical vector wind shear $\partial \vec{V}/\partial h$. Regions where $\mathrm{Ri} < 1.0$ are classed as unstable, while it is generally agreed that $\mathrm{Ri} \leq 0.25$ is required for turbulence initiation. Values of $\mathrm{Ri} < 1.0$ computed from the radiosonde data are indicated in figures 3 to 9 by the solid lines below the $C_N^2(h)$ data. Small values of Ri are achieved with small $(\partial T/\partial h + \gamma_a)$, large $|\partial \vec{V}/\partial h|^2$, or a combination of both. The concept of stable temperature sheets (small negative $\partial T/\partial h$) or inversion layers (positive $\partial T/\partial h$) associated with turbulence seems contradictory to the attainment of low Ri numbers. Actually, as Scorer[12] has pointed out, initial tilting and thickening of the stable sheets could cause very local decreases in Ri numbers, which in turn would permit turbulence onset in an otherwise statically stable environment. Often the wind shear present is sufficient to produce a low Ri number for the sheet or structure as a whole. On this basis we would expect best correlation between small Ri and maxima of $C_N^2(h)$ in those regions where either data set is computed for atmospheric layers of relatively large thickness. This is because of the resolution of $C_N^2(h)$ data (75 m or 150 m) and radiosonde data (300 m). Local decreases in Ri occurring in thin layers would not be resolved. Reiter and Lester[13] have demonstrated the striking dependence of calculated Ri value on the altitude interval used in gradient calculations. From their evidence it is quite possible that if higher resolution meteorological data were available, the computed Ri could decrease to values less than 0.25 and predict directly the observed turbulence. As it is, the computed Ri values are typically large, rarely droping below 1.0 or entering the critical region below 0.25. Regions where they do are well correlated with $C_N^2(h)$ maxima. Good examples of this behavior are found at the 11.1-km level of flight 5 and the 2.2-km level of flight 9. These could be examples of well developed turbulence where the Ri number is reduced for the structure as a whole. In other regions minima in Ri, while not less than 0.25, do occur at the same altitude as $C_N^2(h)$ peaks. These regions suggest the need for higher resolution meteorological data.

The $C_N^2(h)$ data characteristics of strong thin layers, well correlated with the presence of temperature inflections, stable layers and wind shear, tend to support the explanation for high altitude turbulence generation in terms of breaking wave motion and Kelvin-Helmholtz instability. The interested reader is referred to Scorer[12] and Woods[14] for readable accounts of the turbulence theory. The essential points of the theory are as follows. Stable stratification or layers in the atmosphere occur at the boundary between air masses or as an upper limit for convective activity. Wind shear frequently is present or develops across this layer boundary. Internal gravity waves (IGW), induced by air flow over even minor terrain features, propagate continuously through the troposphere. Upon reaching higher altitudes and thus lower densities, the IGW increase in amplitude due to conservation of energy. Either the IGW or large vertical wind shear components tend to tilt the stable temperature layers in a periodic fashion. Often the result of this tilt would be a simple sinusoidal shape for the stable layer. The tilted layer would typically have an initial thickness of a few tens of meters, amplitude and wavelength of hundreds of meters, and horizontal extent of several kilometers. Examples of this action appear in the periodic cloud patterns that occur at various levels in the troposphere and are easily visible to the human eye at ground level. The clouds act as tracers to make visible the tilting phenomena which occurs predominately in clear air above convective activity. The roughly sinusoidal layers formed by tilting are called Kelvin-Helmholtz rolls or billows. While IGW are always present in the atmosphere, they predominate in the lee of wind flow over mountains. Thus strong turbulence should be associated with mountainous terrain. Excellent support for turbulence in these mountain waves was found in the White Sands Missile Range thermosonde data reported by Bufton[8].

As the billows develop they tend to overturn and become dynamically unstable. The overturning is analogous to the behavior of ocean waves approaching the shore. Wave troughs tend to recede opposite to the direction of mean flow, while wave crests are proceeding in the direction of mean flow. The result is a thickened layer where troughs and crests meet. As the wave proceeds the crests overturn, a curl develops, and the wave breaks into turbulent activity. It is the thickening of the wave as trough meets crest that produces instability. As Scorer[12] pointed out, $R_i$ is inversly proportional to the square of layer thickness and wind shear. As a result very local decreases in $R_i$ are most likely in thick sections of the layer where shear is present. If $R_i$ becomes less than 0.25, turbulence onset occurs. The turbulence expands to four or five times the original layer thickness, acquiring energy by feeding on the available wind shear.

As a consequence of the turbulent mixing,two new stable layers are created, at the top and at the bottom of the original but now thickened and turbulent layer. As time progresses the two stable layers can also break down into turbulent activity, while the original turbulence dies away due to depletion of input wind shear. Good examples of this behavior appear to be present in the $C_T^2(h)$ data of figures 6 and 9. In particular the two strong layers of $C_T^2(h)$ at 9.2 and 10.1 km in figure 9 on either side of the strong shear at 10.7 km may be a fine example of a later state of turbulence development.

### Comparisons with Stellar Observations

The first flight series of the new thermosonde payload were accompanied by nearly simultaneous stellar observations with a ground-based telescope. The major motivation for this work was the desire to predict observed optical statistics by means of measured turbulence structure and current optical propagation theory. The side-by-side comparison of turbulence and optical data is illustrated in the experiment concept of figure 10. Although the optical propagation data were generated by observations of bright stars near zenith, the propagation link is identical to direct detection of down-link laser radiation from a source in space. The $C_N^2(h)$ profiles and comparisons with propagation statistics in this experiment serve to

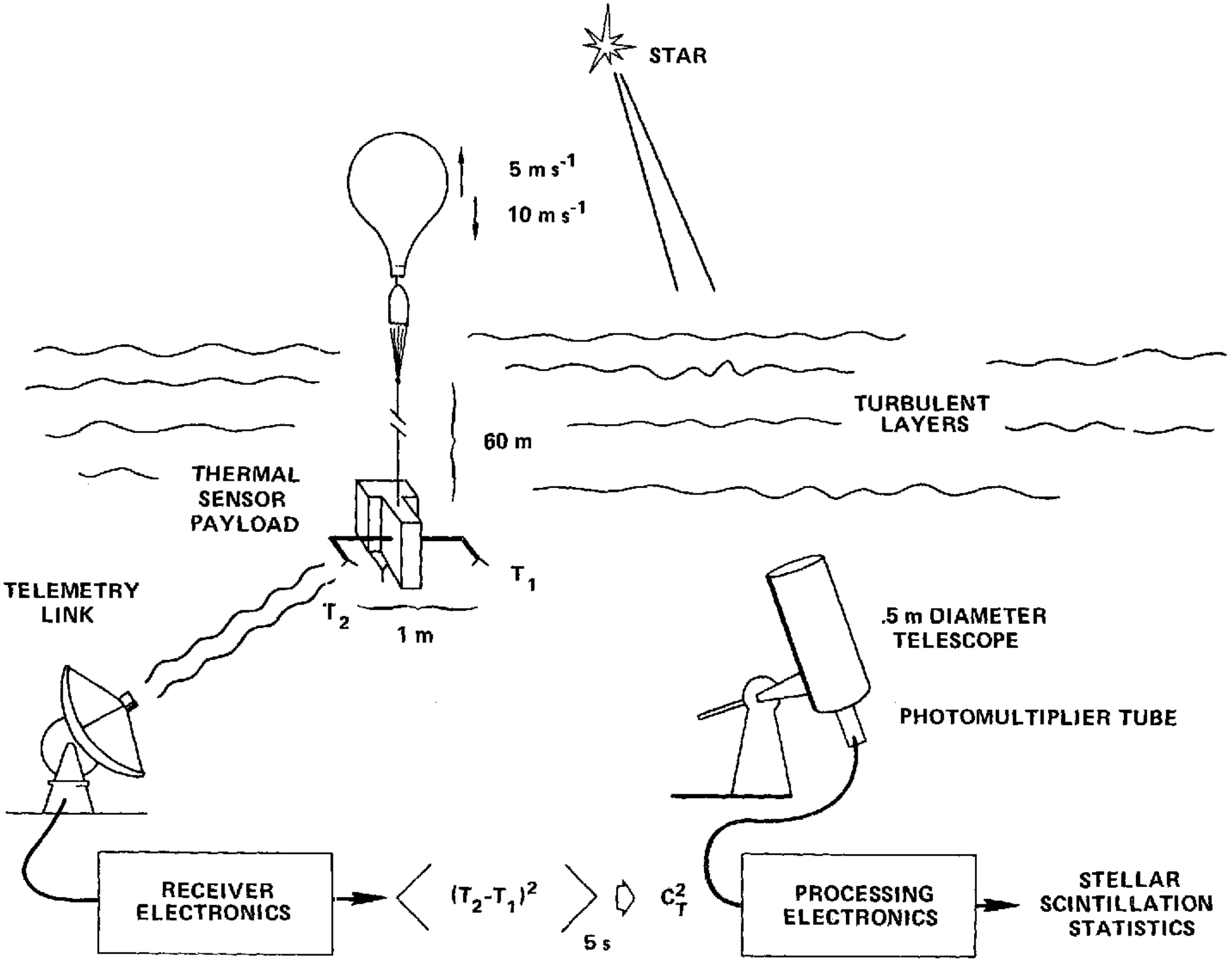

Figure 10. Experiment Concept for Comparison of Stellar and Turbulence Data

illustrate the application of the thermosonde technique. Turbulence structure at the tropopause has traditionally been held to be the major cause of stellar scintillation. The evidence at hand both from radar studies and the present thermal sensor data suggest that while strong turbulence is often correlated with the tropopause, other regions, in particular, the lower troposphere, exhibit large values of $C_N^2(h)$. The important question to resolve is whether the weight assigned to $C_N^2(h)$ versus h by the theory for prediction of scintillation statistics is necessary and sufficient to predict these same statistics.

The stellar and turbulence data presented here were obtained on several clear nights during July, August, and September 1972 at the Goddard Optical Research Facility. The balloon flight plus simultaneous optical observations were conducted within 1 to 2 hours of the regularly scheduled National Weather Service radiosonde flight from Sterling, Virginia at 00:15 GMT. The standard radiosonde flight provided temperature, pressure, and wind velocity profiles for interpretation of the turbulence and optical data. Each turbulence profile used in this analysis was a composite of descent data and ascent data. Ascent data were used only as necessary to fill in the gap below 1 or 2 km caused by telemetry loss on descent. A preference for descent data results from the desire to eliminate wake effects, or false turbulence readings, from the data.

Optical propagation data consisted of measurements of stellar scintillation and were obtained with a 50 centimeter (20-inch) reflector telescope with aperture stopped down to a clear 17.7-centimeter aperture. An EMI 9558B photomultiplier tube (PMT) was located in the telescope focal plane and provided the raw stellar data. An optical filter together with the PMT S-20 photocathode restricted the optical bandpass to 150 nm centered at 520 nm. Figure 11 is a block diagram of the scintillation monitor for both day and night operation. A more detailed description of the detector head is presented by Bufton and Genatt.[15] Analog processing electronics were used to compute the fractional modulation of scintillation (MOD),

$$\text{MOD} = \frac{\text{true rms irradiance}}{\text{(average - background) irradiance}} . \tag{4}$$

The raw stellar data were also fed into a real time spectral analyzer and digital integrator. Spectral analysis was from 0.16 Hz to 200 Hz with a 1-Hz resolution. Typical data run length was two minutes. The results were the strength of irradiance fluctuations (scintillation) and their temporal spectra.

Optical propagation theory for the stellar observation case is cast in terms of integrals over the $C_N^2(h)$ turbulence structure. Thus the first step in comparison of the two data sets was computation of the required integrals. These integrals were computed numerically by summation of $C_N^2(h)$ points separated by an altitude interval of 150 m. For the typical descent rate of 10 m $s^{-1}$ and data time constant of 5 seconds, each $C_N^2(h)$ point was an average over three vertical resolution elements.

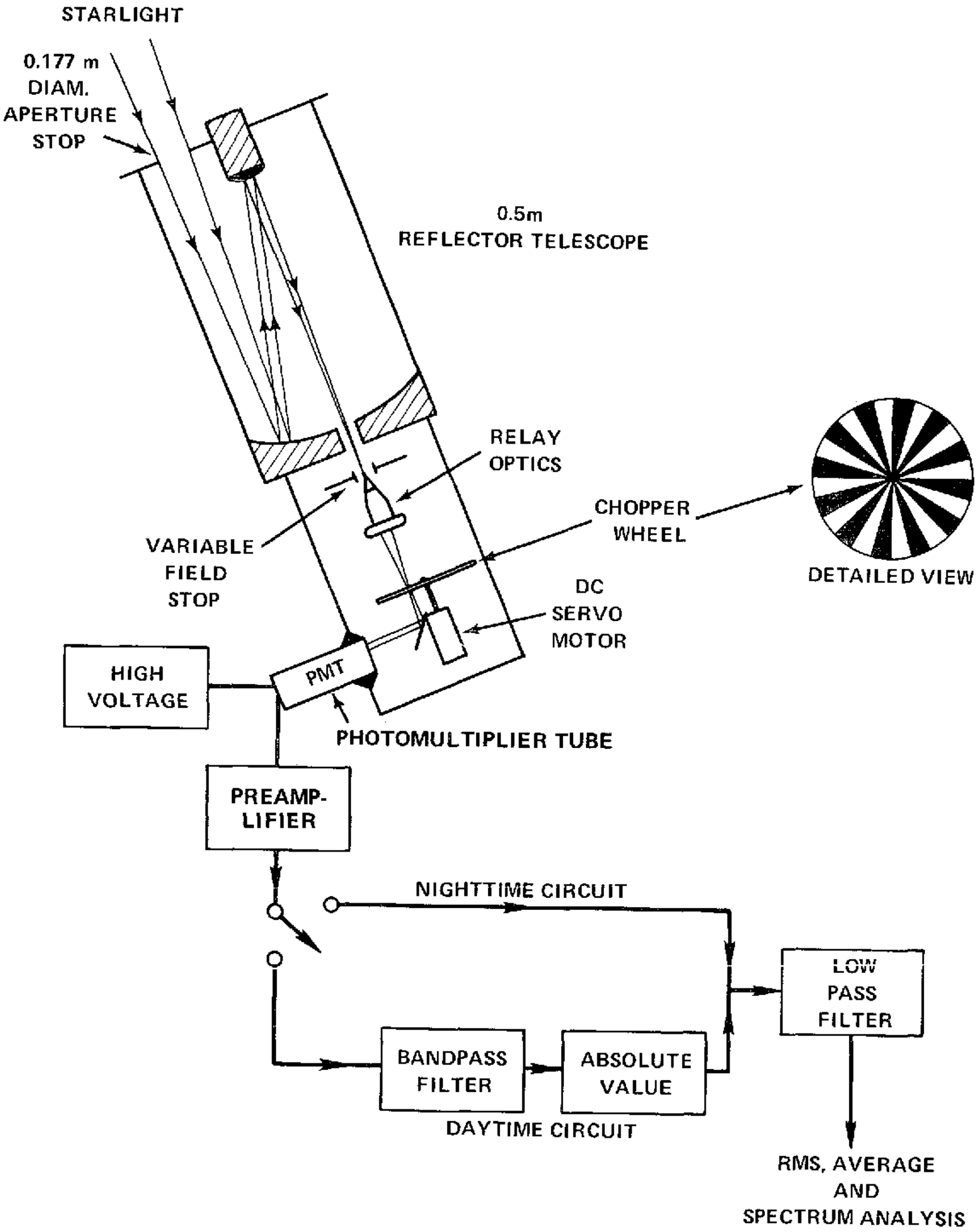

Figure 11. Scintillation Monitor for Day and Night Observations

The first integral,

$$I_1 = \int_{h_0}^{h_{max}} C_N^2(h)\, dh, \qquad (5)$$

is a linear weighting and sum over $C_N^2(h)$ at all altitudes from surface level, $h_0$, to the maximum altitude, h, of reported data for the particular flight. An integral of this form appears in the theoretical description of optical wavefront statistics for plane wave propagation of starlight to a ground receiver. An estimate of $I_1$ can be derived from the Tatarski[16] result for image motion variance,

$$\sigma_m^2 = K_1\, D^{-1/3} \sec\theta \int_0^\infty C_N^2(h)\, dh, \qquad (6)$$

with the additional assumptions that,

$\theta$ = stellar zenith angle = 0°
D = aperture diameter = 0.177 m
$K_1 \lesssim 2.91$
$\sigma_m^2$ = 0.5 arc sec$^2$ (typical result for $\theta$ = 0° and D = 0.177 m)

The result is a prediction that

$$I_1 \gtrsim 4.7 \times 10^{-13} m^{1/3}$$

The $I_1$ integrals computed from the $C_N^2(h)$ data profiles are listed in table 3. The agreement between predicted and observed values is with a factor of 2 to 4. Contribution to $I_1$ from the surface boundary layer (first 10 m) ranged from 22 percent for flight 6, to 47 percent for flight 9. The factor of 2 to 4 agreement seems quite good considering the lack of direct measurement of $\sigma_m^2$ and the uncertainty in the value of $K_1$ from the theory.

The irradiance statistic MOD is found in the wave optical treatment of stellar irradiance statistics of Tatarski.[16] It can be squared and written as–

$$MOD^2 = K_2 \sec^\gamma \theta\, I_2, \qquad (7)$$

for observations at stellar zenith angle $\theta$. Theory yields the value $\gamma = 3.0$ for zenith angle dependence in the limit of a large telescope aperture. The experimental data of Protheroe[17] can be used to estimate $\gamma = 2.5$ for D = 0.177 m. $I_2$ is the second integral,

$$I_2 = \int_{h_0}^{h_{max}} C_N^2(h)\, h^{5/6} dh, \qquad (8)$$

Table 3

Comparison of Integrals Over $C_N^2(h)$ and Fractional Modulation Squared ($MOD^2$) Values as Computed from Thermal Sensor (Comp) and Optical Data (Data)

| Flight Number | $h_{max}$ (km) | $I_1$ $(m^{1/3}) \times 10^{12}$ | $I_2$ $(m^{7/6}) \times 10^9$ | $I_3$ $(m^{7/3}) \times 10^5$ | $MOD^2_{Data}$ | Zenith Angle (degrees) | $MOD^2_{Comp}$ |
|---|---|---|---|---|---|---|---|
| 4 | 18.3 | 1.8 | 1.1 | 5.9 | 0.18 | 37 | 0.13 |
| 6 | 20.2 | 1.0 | 1.2 | 6.3 | 0.21 | 34 | 0.13 |
| 7 | 24.4 | 1.4 | 0.85 | 3.8 | 0.33 | 66 | 0.61 |
| 9 | 24.1 | 1.8 | 1.6 | 7.7 | 0.21 | 14 | 0.10 |

over $C_N^2(h)$ turbulence structure weighted by the 5/6 power of altitude. The $K_2$ proportionality "constant" includes wavelength dependence, aperture averaging factor and numerical scaling. No attempt is made here to report or derive $K_2$ from the theory, since additional data on the irradiance correlation length is required in order to accurately predict aperture averaging. Atmospheric dispersion effects discussed by Young[18] would also have to be taken into account. These effects influence the data because of the 150 nm optical bandpass and observation at angles other than zenith. Values for $I_2$ computed in a similar numerical fashion to those for $I_1$ are listed in table 3. Also included there are the corresponding $MOD^2_{Data}$ values and the zenith angle of observation. The average ($1.2 \times 10^{-9}$ $m^{-7/6}$) of the four $I_2$ values compares roughly with a value of $6.0 \times 10^{-10} m^{-7/6}$ reported by Hulett[19] on the basis of widely scattered scintillation measurements. The trend in $I_2$ among the flights is repeated by the scintillation data with only little relative scatter. This argues for data validity. The departure of the two data sets from a one-to-one correspondence may be explained by the aperture averaging and dispersion effects noted above. These effects are probably most severe for the flight 7 $MOD^2_{Data}$ data taken at $\theta = 66°$.

The temporal spectrum of the irradiance pattern sampled by the telescope aperture provides another test of data and theory. Aperture averaging and zenith angle dependences appear clearly in the analytical result. In this test the $C_N^2(h)$ profiles plus the wind speed normal to the stellar line of sight are inserted into the theory and the result is compared with irradiance spectral density data.

The normal wind speed component was obtained from the vector winds reported by radiosonde. The conversion, as reported by Young,[18]

$$V_N(h) = V_0(h) \cos\theta \, [1 + \tan^2\theta \sin^2(\beta - \alpha)]^{1/2}, \tag{9}$$

employs wind speed $V_0$ (h), wind direction $\alpha$, stellar zenith angle $\theta$, and stellar azimuth $\beta$.

The theory is derived according to the method of Tatarski.[16] The starting point is his equation (13.38) for irradiance frequency spectrum in terms of the two-dimensional spatial spectrum of irradiance and a filter function for a ciruclar unobstructed aperture. The form below is obtained for the vertical propagation path:

$$W_I(f) = 2.11\pi^2 k_0^2 \int_0^\infty \frac{C_N^2(z)}{V_N(z)} \int_0^\infty [\kappa^2 + 4\pi^2 f^2/V_N^2(z)]^{-11/6}$$

$$\sin^2\left[\frac{(\kappa^2 + 4\kappa^2 f^2/V_N^2(z))\,z}{2k_0}\right]\left[\frac{2J_1\left(D/2\sqrt{\kappa^2 + 4\pi^2 f^2/V_N^2(z)}\right)}{D/2\sqrt{\kappa^2 + 4\pi^2 f^2/V_N^2(z)}}\right]^2 d\kappa\, dz, \qquad (10)$$

where:

$W_I$ (f) = irradiance spectral density,
$V_N$ = component of wind velocity normal to the propagation path,
$\kappa$ = spatial frequency in aperture plane,
f = temporal frequency,
D = aperture diameter, and
$k_0$ = $2\pi/\lambda_0$ = optical propagation constant.

This result states that the amplitude of irradiance spectral density at each frequency is a linear combination of $C_N^2$(h) weighted by inverse wind speed and a sum over the spatial spectrum of turbulence, a diffraction term, and aperture filter function.

The integrals of equation (10) were computed numerically on a digital computer after insertion of the observed $C_N^2$(h) and $V_N$(h) profiles, the 0.177 m aperture and the stellar zenith angle. An 8-point Gaussian quadrature formula was used to perform the inner integration. Typical integral limits for this procedure corresponded to a $\kappa_i$ of 6.3 $m^{-1}$ and $\kappa_0$ of 57 $m^{-1}$ for inner and outer limits, respectively. The limits $h_0$ and $h_{max}$ appropriate for each flight were used for the outer integral. The height interval was again 150 m and the standard trapezoidal integration method was used.

Irradiance spectra computed in this manner for flights 6 and 9 are indicated by the solid lines in figure 12. The open and closed circles indicate the corresponding stellar data. Each irradiance data spectrum was computed for a 2-minute segment of data used previously to compute the $MOD_{Data}^2$ values reported in table 1. Note that spectral density functions normalized to unity are plotted. There is quite good agreement between data and prediction under different wind conditions of the two flights. The largest differences occur at low frequencies and for the lower wind speeds of flight 9. Possible error mechanisms at work here may be a breakdown in assumptions of equation (10), truncation of the Kolmogorov spectrum at low spatial frequencies, or too much weighting of high-altitude turbulence.

The constants used to normalize the spectra of figure 12 were computed by integrating $W_I(f)$ of equation (10) over the frequency range of interest. These constants are predictions of $\mathrm{MOD}^2$ based only on the $C_N^2(h)$ and $V_N(h)$ profiles and theory,

$$\mathrm{MOD}^2_{\mathrm{Comp}} = \int_0^{f_{\max}} W_I(f)\,df. \tag{11}$$

The upper limit $f_{\max}$ was set at 200 Hz. Values of $\mathrm{MOD}^2_{\mathrm{Comp}}$ are listed in table 3 for comparison with experimental $\mathrm{MOD}^2_{\mathrm{Data}}$. Agreement between predicted and experimental results is within a factor of two for all flights. The error between the results is a monotonic function of the zenith angle. This suggests the presence of an additional zenith angle dependence in the data, perhaps that due to the dispersion effect noted above. A more detailed discussion of these stellar comparisons with implications for the optical propagation theory is given by Bufton.[20]

### Daytime Turbulence and Stellar Results

Turbulence profiles have also been obtained during the daytime. Figure 8 is a $C_N^2(h)$ daytime profile. Note that while similar in structure for both day and night the turbulence layers appear stronger in the lower atmosphere during the day. This trend is substantiated by the work of other researchers.[1,2] Upper altitude turbulence also appears stronger during the day. Although the sharp inversion layer at 19 km suggests that strong turbulence should be found, it is not possible to be certain that these data are correct. Even if incorrect there would be little net effect on prediction of optical propagation statistics. Further evidence for the validity of these layers will have to wait for the availability of simultaneous optical data during the daytime. Some preliminary daytime stellar observations have been made with a modified version of the nighttime stellar scintillation monitor. They indicate a factor of two increase in scintillation strength (MOD) over average nighttime results. The signal-to-noise ratio for daytime stellar work was improved by a background discrimination technique outlined in figure 11. The incoming stellar radiation and the sky background were chopped at a 2-kHz rate by clear and opaque sectors of a glass disk before detection by the PMT. The field of view was adjusted to just equal one chopping cycle on the glass disk. Thus the amount of background entering the PMT was constant in time despite the chopping action. The raw stellar data from the PMT were then bandpass-filtered to remove the dc background component. A standard AM demodulation technique of an absolute value circuit followed by a low-pass filter recovered the scintillation data.

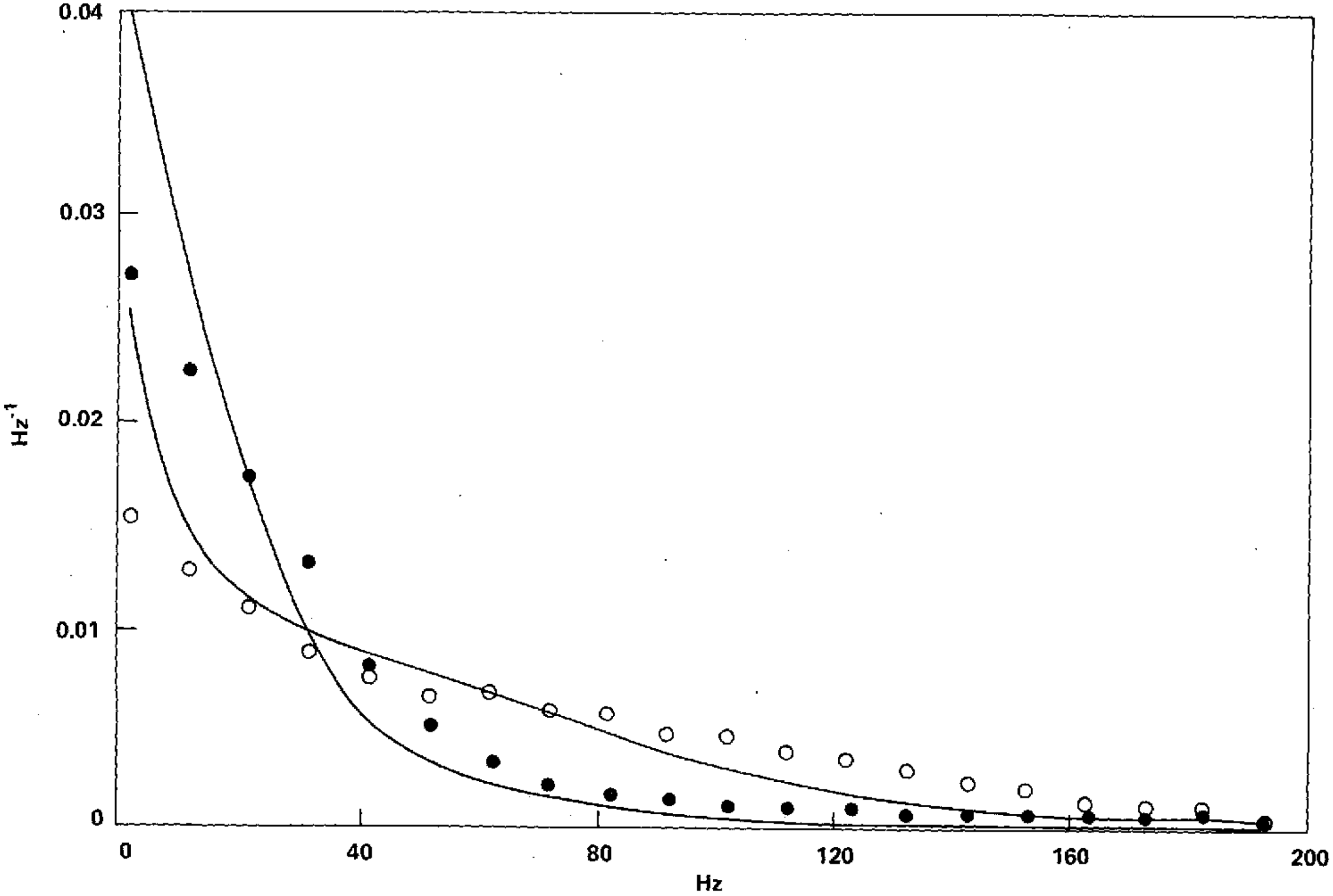

Figure 12. Normalized Spectral Density of Irradiance. (Data for flights 6 (○) and 9 (●) versus frequency. The curves show predicted density, based on $C_N^2$ (h) data of figures 6 and 9.)

The daytime thermosonde measurements have an additional temperature error source in the presence of direct solar radiation. The effect of solar radiation on the thermal sensor element itself is one possible source of $\Delta T$ errors. Solar heating of the probe support structure with transfer of heat to the proble is an additional factor. If both probes are heated equally, no $\Delta T$ error should result. A typical balloon flight, however, involves pendulum motions and payload spin. The results are continuous changes in the solar aspect angle and the possibility of occasional shading of one probe. From the calculations and data reported by Ney, Maas, and Huch[21] the solar radiation error for 2.5-$\mu$m diameter probe wire at high altitude can be estimated at several hundredths of a degree celsius. This can lead to appreciable error in the $C_T^2(h)$ measurements. Radiation effects of this nature are more predominate at high altitude because of less efficient heat removal by convection. As a result the daytime indication of strong turbulence near 20 km and above in figure 8 should be regarded with some suspicion.

### Prediction of Laser Propagation Data

The major application of the microthermal turbulence data ($C_N^2(h)$) to the prediction of laser propagation data is found in the downlink case. Laser radiation orginating in a satellite or spacecraft propagates downward through the entire atmosphere to a receiver station at ground level. The laser link would be used for high-data-rate communication. The ground receiver terminal would take one of two forms: a large photon bucket for direct detection of all possible incident laser radiation, or a heterodyne system for coherent detection. The space terminal is far enough removed that laser radiation is essentially plane wave by the time it reaches atmospheric turbulence. Thus the problem is directly analogous to the stellar observations case described earlier. In direct detection the important information is the irradiance pattern sampled by the telescope aperture. Turbulence data enters through the theoretical prediction of irradiance statistics in terms of

$$\int_0^\infty C_N^2(h)\, h^{5/6}\, dh$$

as in equation (8). In coherent detection, phase information is most important, and the propagation statistics contain integrals of the form

$$\int_0^\infty C_N^2(h)\, dh$$

as in equation (5). A number of interesting propagation statistics can then be formed by inserting the above two integrals into the theory. The two most important statistics are aperture-averaged log-amplitude variance.

$$\sigma_{\ell}{}^{2} = A\,(D, \theta, \sigma_{\ell}{}^{2})\, 0.56\, k^{7/6} \sec\theta^{11/16} \int_{0}^{\infty} C_N^2(h)\, h^{5/6} dh, \tag{12}$$

where:

A = aperture averaging factor,
D = aperture diameter,
$\theta$ = stellar zenith angle,
k = optical wave number and
h = altitude,

for the direct detection case and coherence aperture diameter; and

$$r_0 = 1.2 \times 10^{-8}\, \lambda^{6/5} \left[ \int_{0}^{\infty} C_N^2(h)\, dh \right]^{-3/5} (\cos\theta)^{3/5}, \tag{13}$$

where:

$\lambda$ = wavelength in microns,
$\theta$ = stellar zenith angle and
h = altitude,

for the coherent case.

The uplink laser propagation case is also of interest for laser beacon and communication link possibilities. The primary statistic is received log-amplitude variance. Although the $h^{5/6}$ dependence is still present, the plane wave assumption is no longer valid. Account must be taken of transmitter beam size and divergence. Titterton[22] has indicated that the finite beam property may be used to reduce uplink scintillation by focusing the beam on the region of major turbulence in the upper atmosphere. Obviously the location and strength of turbulence layers are extremely important for this analysis.

A further application involves resolution looking down through the atmosphere from a space platform. This has relevance to the areas of reconnaissance and remote sensing. Fried[23] indicates that resolution should be proportional to the integral

$$\int_{0}^{\infty} C_N^2(h)\, h^{5/3}\, dh. \tag{14}$$

This integral plus the two shown previously must be evaluated for quantitative prediction of the desired propagation statistics. In the present comparison of stellar observations and turbulence data reported here, the many data points of each $C_N^2(h)$ profile were inserted and the integration performed numerically. It would be much simpler to assume a model for $C_N^2(h)$, perform the required integration analytically, and then adjust the model parameters to account for the time distribution and strength of turbulence.

Numerous authors have suggested an exponential decrease in $C_N^2(h)$ with a separate maximum or bump to account for upper altitude effects. This in effect establishes an envelope for the behavior of multiple turbulence layers. As an example the profile could be written

$$C_N^2(h) = A\frac{\exp(-h/H_0)}{h^\alpha} + B\exp\left[-\frac{(h-H_1)^2}{2\beta^2}\right]. \tag{15}$$

The parameters A, $\alpha$, $H_0$, B, $\beta$ and $H_1$ could be estimated from the thermosonde data by noting the relative strength of turbulence in adjacent atmospheric regions. A more tractable model might be a series of delta function ($\delta$) layers at regular height intervals (e.g., 1 km),

$$C_N^2(h) = \sum_i A_i\,\delta(h-h_i). \tag{16}$$

Delta function amplitude ($A_i$) would be adjusted to correspond to thermosonde data in the neighborhood of altitude $h_i$. The appropriate integrals are easily evaluated with delta functions in place of exponential and altitude power low dependencies. Fortunately altitude dependence of the propagation statistics is not critical on exact turbulence location. Accuracies within a km or so are sufficient.

## Application to CAT Detection

In the current research $C_T^2(h)$ results are used to compute strength of refractive-index fluctuations $C_N^2(h)$ and thus the optical effects of atmospheric turbulence. These same temperature fluctuations are, in fact, just evidence of density inhomogenities in the atmosphere. Since the atmosphere will not support local pressure gradients, warm parcels of air must be less dense than cold parcels at the same altitude. Thus temperature acts as a tracer for density and $C_T^2(h)$ acts as a tracer for turbulence-induced density fluctuations. Density fluctuations in the range 20 m to 200 m form the clear air turbulence (CAT) that adversely effects aircraft operations. The small scale (of order 1 m) microthermal fluctuations measured by the thermosonde technique in terms of $C_T^2(h)$ depend for their existence on the cascade of turbulent energy from the larger scale structures. The correlation between small scale turbulence and large scale turbulence (CAT) has been demonstrated by recent radar studies of the upper atmosphere. In several cases[24 25] the radar observations (sensitive to turbulence dimensions of order 30 cm) have corresponded to simultaneous aircraft encounters with clear air turbulence.

In addition, the thermosonde data show consistent correlation between regions of high dynamic instability (Kelvin-Helmholtz billows) and $C_T^2(h)$ peaks. The Kelvin-Helmholtz billows are considered a fundamental origin for CAT effects. The best application of the thermosonde technique to the CAT detection role would be, first of all, in side-by-side operation with groundbased CAT radar systems. Then it may be desirable to launch thermosondes from standard radiosonde sites on a systematic basis to monitor a heavily traveled air corridor, and compare the data with aircraft turbulence encounters. Furthermore, once the spectral shape for turbulence wavenumbers is known, the strength of small scale turbulence can be used to predict quantitatively the strength of CAT. There is considerable experimental evidence to suggest that the predominate spectral shape is the (-5/3) power of wavenumber predicted by the Obukhov-Kolmogorov theory for the inertial subrange.

## COMMENTS

The microthermal profile measurements reported here suggest that upper altitude turbulence structure is concentrated in various layers. While the strongest layers of turbulence were found at the surface boundary layer and associated with temperature inflections and shear layers in lower troposphere, significant contributions to $C_N^2(h)$ were recorded from the tropopause region and occasionally from the stratosphere. It is the strong correlations with meterological parameters and the predictable cascade of energy from large to small structures that suggest the application of the thermosonde to CAT detection. The observed turbulence combined with current theory works well to predict not only strength of scintillation, but also the observed temporal spectra, if wind velocity profile data are included. Agreement is good between prediction and data despite the expected non-stationarity of turbulence. The present method of differential thermal sensor measurements from a balloon payload yields vertical cross sections of a $C_N^2(h)$ structure that varies widely in time and space. Because of the horizontal sheet nature of this structure the thermal sensor data should be a reasonable first estimate of $C_N^2(h)$ strength and distribution. If the application is limited to comparison with simultaneous optical propagation data, results within a factor of two should be expected. More accurate comparisons, prediction, and tests of propagation theory will require three-dimensional measures of turbulence in addition to the profile samples.

The most pressing need in future investigations is a measurement program for turbulence spatial spectrum in the upper atmosphere. Until the presence of an inertial subrange and the validity of Obukhov-Kolmogorov statistics is verified, few quantitative comparisons can be accepted. It will also be necessary to define the limits of non-stationarity of upper altitude turbulence in order to extrapolate the point thermal measurements. Finally the same comparisons of turbulence and optical data should be made during daylight hours to assess the effect of diurnal variations in turbulence strength at high altitude.

Since the first publication of this material in November, 1973, as a GSFC X-document[26] two extremely important and related turbulence measurement programs have been reported in the literature. These independent programs are the work of Coulman[27] and Barletti et al.[28] The reported measurements are quite similar to those of the thermosonde device, in that microthermal-sensor equipped radiosondes were used to obtain the turbulence profile data. The major significance of these efforts is the direct telemetry of raw turbulence data to the ground for subsequent data analysis. The latter two references should be consulted for interpretation of and additional insight into the results reported here.

## ACKNOWLEDGMENTS

The author wishes to express his sincere thanks to Paul J. Titterton, L. E. Mallery, and T. A. Arken. GTE-Sylvania, for design and development of the lightweight thermosonde payload and to David A. Grolemund of RCA for assistance in payload preparation and flight tests.

Goddard Space Flight Center
National Aeronautics and Space Administration
Greenbelt, Maryland February 1974
502-23-15-30-51

## REFERENCES

1. Tsvang, L., "Microstructure of Temperature Fields in the Free Atmosphere," *Radio Science,* **4** (12), December 1969, pp. 1175-1177.

2. Lawrence, R. S., G. R. Ochs, and S. F. Clifford, "Measurements of Atmospheric Turbulence Relevant to Optical Propagation," *J. Optical Soc. Am.*, **60** (6), 1970, pp. 826-830.

3. Minott, P. O., J. L. Bufton, and M. W. Fitzmaurice, *Results of the Balloon Atmospheric Propagation Experiment Flights of 1970 (BAPE I),* NASA TM X-65952, March 1972.

4. Bufton, J. L., P. O. Minott, M. W. Fitzmaurice, and P. J. Titterton, "Measurements of Turbulence Profiles in the Troposphere," *J. Optical Soc. Am.*, **62** (9), September 1972, pp. 1068-1070.

5. Obukhov, A. M., "On the Distribution of Energy in the Spectrum of Turbulent Flow," *Doklady Akad, Nauk SSSR*, 32 (4), 1941, pp. 19.

6. Kolmogorov, A. N., "Dissipation of Energy in Locally Isotropic Turbulence," *Doklady Akad, Nauk SSSR*, 32, 1941.

7. Titterton, P. J., L. E. Mallery, and T. A. Arken, *Lightweight Thermosonde System Final Report* (Contract NAS5-11493), GTE-Sylvania, December 1971.

8. Bufton, J. L., "Correlation of Microthermal Turbulence Data with Meteorological Soundings in the Troposphere," *J. Atm. Sciences*, **30** (1), January 1973, pp. 83-87.

9. Hardy, K. R., and I. Katz, "Probing the Clear Atmosphere with High Power, High Resolution Radars," *Proc. IEEE*, **57** (4), April 1969, pp. 468-480.

10. Doviak, R. J., J. Goldhirsh, and A. R. Miller, "Bistatic-Radar Detection of High-Altitude Clear-Air Atmospheric Targets," *Radio Science*, **7** (11), November 1972, pp. 993-1003.

11. Gossard E. E., D. R. Jensen, and J. H. Richter, "An Analytical Study of Tropospheric Structure as Seen by High-Resolution Radar," *J. Atm. Sciences*, **28**. July 1971, pp. 794-807.

12. Scorer, R. S., "Billow Mechanics," *Radio Science*, **4** (12), December 1969, pp. 1299-1308.

13. Reiter, E. R.,and P. F. Lester, "Richardson's Number in the Free Atmosphere," *Arch. Met. Geoph. Biokl.*, Ser. A, 17, 1968, pp. 1-7.

14. Woods, J. D., "On Richardson's Number as a Criterion for Laminar-Turbulent-Laminar Transition in the Ocean and Atmosphere," *Radio Science*, 4 (12), December 1969.

15. Bufton, J. L., and S. H. Genatt, "Simultaneous Observations of Atmospheric Turbulence Effects on Stellar Irradiance and Phase," *Astronomical J.*, **76** (4), May 1971, pp. 378-386.

16. Tatarski, V. I. (R. A. Silverman, Trans.), *Wave Propagation in a Turbulent Medium*, McGraw-Hill, New York, 1961.

17. Protheroe, W. M., *Preliminary Report on Stellar Scintillation*, Scientific Report 4 (AF 19 (604) - 41, ASTIA No. AD 56040), Physics and Astronomy Dept., Ohio State Univ., November 1954.

18. Young, A. T., "Photometric Error Analysis. VIII. the Temporal Power Spectrum of Scintillation," *Applied Optics*, **8** (5), May 1969, pp. 869-891.

19. Hulett, H. R., "Turbulence Limitations in Photographic Resolution of Planet Surfaces," *J. Optical Soc. Am.*, **57** (11), November 1967, pp. 1335-1338.

20. Bufton, J. L., "Comparison of Vertical Profile Turbulence Structure with Stellar Observations," *Applied Optics*, **12** (8), August 1973, pp. 1785-1793.

21. Ney, E. P., R. W. Maas, and W. F. Huch, "The Measurement of Atmospheric Temperature," *J. Meteorology*, 18, February 1961, pp. 60-80.

22. Titterton, P. J., "Scintillation and Transmitter Aperture Averaging over Vertical Paths," *J. Optical Soc. Am.*, **63** (4), April 1973, pp. 439-444.

23. Fried, D. L., "Limiting Resolution Looking Down Through the Atmosphere," *J. Optical Soc. Am.*, **56** (10), October 1966, pp. 1380-1384.

24. Glover, K. M., J. B. Roland, H. Ottersten, and K. R. Hardy, "Simultaneous Radar, Aircraft and Meteorological Investigations of Clear Air Turbulence," *J. Appl. Meteorology*, 8, August 1969, pp. 623-640.

25. Hicks, J. J., "Radar Observations of a Gravitational Wave in Clear Air Near the Tropopause Associated with CAT," *J. Appl. Meteorology*, 8, August 1969, pp. 627-633.

26. Bufton, Jack L., *Radiosonde Thermal Sensor Technique for Measurement of Atmospheric Turbulence,* NASA TM X-70556, November 1973.

27. Coulman, C. E., "Vertical Profiles of Small-scale Temperature Structure in the Atmosphere," *Boundary-Layer Meteorology,* **4**, April 1973, pp. 169-177.

28. Barletti, R. et al., *Radiosonde Site Testing Campaign at Tenerife (1973),* Joint Organization for Solar Observations (Report No. JOSO SIT 21), Florence, Italy, February 1974.

NASA-Langley, 1975